1 **Spatio-temporal variability of snow water equivalent in the extra-tropical Andes**

2 **cordillera from distributed energy balance modeling and remotely sensed snow**

3 **cover.**

4

5 Edward Cornwell[1], Noah P. Molotch[2,3] and James McPhee*[1,4]

6 *1: Advanced Mining Technology Center, Facultad de Ciencias Físicas y Matemáticas,*
7 *Universidad de Chile*
8 *2: Department of Geography and Institute of Arctic and Alpine Research, University of*
9 *Colorado, Boulder*
10 *3: Jet Propulsion Laboratory, California Institute of Technology, Pasadena, California,*
11 *USA.*
12 *4: Departamento de Ingeniería Civil, Facultad de Ciencias Físicas y Matemáticas,*
13 *Universidad de Chile*
14
15 **: corresponding author: jmcphee@u.uchile.cl*
16

17 **Abstract**

18 Seasonal snow cover is the primary water source for human use and ecosystems along

19 the extratropical Andes Cordillera. Despite its importance, relatively little research has

20 been devoted to understanding the properties, distribution and variability of this natural

21 resource. This research provides high-resolution (500-meter), daily distributed estimates

22 of end-of-winter and spring snow water equivalent over a 152,000-km^2 domain that

23 includes the mountainous reaches of central Chile and Argentina. Remotely sensed

24 fractional snow covered area and other relevant forcings are combined with extrapolated

25 data from meteorological stations and a simplified physically-based energy balance

26 model in order to obtain melt-season melt fluxes which are then aggregated to estimate

27 end-of-winter (or peak) snow water equivalent (SWE). Peak SWE estimates show an

28 overall coefficient of determination R^2 of 0.68 and RMSE of 274 mm compared to

29 observations at 12 automatic snow water equivalent sensors distributed across the model

30 domain, with R^2 values between 0.32 and 0.88. Regional estimates of peak SWE

accumulation show differential patterns strongly modulated by elevation, latitude and position relative to the continental divide. The spatial distribution of peak SWE shows that the 4000 - 5000 m.a.s.l. elevation band is significant for snow accumulation, despite having a smaller surface area than the 3000 – 4000 m.a.s.l. band. On average, maximum snow accumulation is observed in early September in the western Andes, and in early October on the eastern side of the continental divide. The results presented here have the potential of informing applications such as seasonal forecast model assessment and improvement, regional climate model validation, as well as evaluation of observational networks and water resource infrastructure development.

1   Introduction

Accurately predicting the spatial and temporal distribution of snow water equivalent (SWE) in mountain environments remains a significant challenge for the scientific community and water resource practitioners around the world. The Andes Cordillera, a formidable mountain range that constitutes the backbone of the South American continent, remains one of the relatively least studied mountain environments due to its generally low accessibility and complex topography. The extratropical stretch of the Andes, extending south from approximately latitude 27 º S, is a snow-dominated hydrological environment that provides key water resources for a majority of the population in Chile and Argentina. Until now, a very sparse network of snow courses and automated snow measuring stations (snow pillows) has been the only source of information about this key resource. In a context of sustained climate change characterized by warming trends and likely future precipitation reductions (Vera et al., 2006; Vicuña et al., 2011), it becomes ever more relevant to understand the past dynamics of the seasonal snowpack in order to validate predictive models of future

56 snow-water resources. This research presents the first spatially and temporally explicit

57 high-resolution SWE reconstruction over the snow-dominated extratropical Andes of

58 central Chile and Argentina based on a physical representation of the snowpack energy

59 balance (Kustas et al., 1994) and remotely sensed snow extent (Dietz et al., 2012)

60 between years 2001 and 2014. A key advantage of the presented product is its

61 independence from notoriously scarce and unreliable precipitation measurements at

62 high elevations. Estimates of maximum SWE accumulation and depletion curves are

63 obtained at 500-m resolution, coincident with the MODIS Fractional Snow Cover

64 product MOD10A1 (Hall et al., 2002).

65 Patterns of hydroclimatic spatiotemporal variability in the extratropical Andes have

66 been studied with increased intensity over the last couple of decades, as pressure for

67 water resources has mounted while at the same time rapid changes in land use and

68 climate have highlighted the societal need for increased understanding of water resource

69 variability and trends under present and future climates. The vast majority of studies

70 have relied on statistical analyses of instrumental records and regional climate models

71 to present synoptic-scale summaries of precipitation (e.g. Aravena and Luckman, 2009;

72 Falvey and Garreaud, 2007; Garreaud, 2009), temperature (Falvey and Garreaud, 2009),

73 snow accumulation (Masiokas et al., 2006) and streamflow variability (Cortés et al.,

74 2011; Núñez et al., 2013). Currently, no high-resolution, large-scale distributed

75 assessments of snow water equivalent are available for the Andes region.

76 The SWE reconstruction method seeks to estimate end-of-winter accumulation by back

77 accumulating melt energy fluxes during the depletion season. The methods and

78 assumptions required for SWE reconstruction have been tested and refined since initial

79 development (Cline et al., 1998). Applications across a variety of scales have been

80 presented in recent years. In the Sierra Nevada, Jepsen et al. (2012) compared SWE

81   reconstructions to distributed snow surveys in a 19.1 km^2 basin (R^2 = 0.79), while Guan

82   et al. (2013) obtained good correlation with SWE observations from an operational

83   snow sensor network across the entire Sierra Nevada   (R^2 = 0.74). In the Rocky

84   Mountains, Jepsen et al. (2012) obtained an R^2 value of 0.61 when comparing

85   reconstructed SWE to spatial regression from snow surveys, and Molotch (2009)

86   estimated SWE with a mean absolute error (MAE) of 23% compared to intensive study

87   areas. A useful discussion on the uncertainties of the SWE reconstruction method -albeit

88   one based on temperature-index melt equations- was presented by Slater et al. (2013),

89   who demonstrated that errors in forcing data are at least, if not more, important than

90   snow covered area data availability. The vast majority, if not all, of SWE reconstruction

91   exercises have been developed in the northern hemisphere, under environmental

92   conditions quite different from those predominant in the extratropical Andes Cordillera.

93   Here, snow distribution and properties have been analyzed in a few local studies (e.g.

94   Ayala et al., 2014; Cortés et al., 2014; Gascoin et al., 2013), but no large-scale

95   estimations at a relevant temporal and spatial resolution for hydrologic applications

96   have been presented. In fact, the Andes of Chile and Argentina display near-ideal

97   conditions for the SWE reconstruction approach due to (1) the near absence of forest

98   cover over a large fraction of the domain where snow accumulation is hydrologically

99   significant; (2) the sharp climatological distinction between wet (winter: June through

100   August) and dry (spring/summer: September through March) seasons, with most of

101   annual precipitation falling during the former; and (3) the low prevalence of cloudy

102   conditions during spring and summer months over the mountains, which afford a high

103   availability of remotely sensed snow cover information. Conversely, the SWE

104   reconstruction presented here is certainly subject to a series of uncertainty sources, such

105   as the sparseness of the hydrometeorological observational network, which limits both

106   the availability of forcing and validation data.

107   However, this is the first estimation of peak SWE and snow depletion distribution at

108   this scale and spatial resolution for the extratropical Andes, and the information shown

109   here can be useful for several applications such as understanding year-to year

110   differential accumulation patterns that may impact the performance of seasonal

111   streamflow forecast models that rely on point-scale data only. Also, the SWE

112   reconstruction can be used to validate output from global or regional climate models

113   and reanalysis, which are being increasingly employed to estimate hydrological states

114   and fluxes in ungauged regions. By analyzing the spatial correlation of snow

115   accumulation and hydrometeorological variables, distributed SWE estimates can inform

116   the design of improved climate observation networks. Likewise, from analyzing the

117   obtained SWE estimates in light of the necessary modeling assumptions and data

118   availability we are able to highlight future research directions aimed at quantifying and

119   reducing these uncertainties.

120   The objectives of this research include: 1) To assess the dominant patterns of spatio-

121   temporal variability in snow water equivalent of the snow-dominated extratropical

122   Andes cordillera; and, 2) to explicitly evaluate the strengths and weaknesses of the

123   SWE reconstruction approach in different sub-regions of the extratropical Andes using

124   snow sensors and distributed snow surveys.

125   **2   Study Area**

126   Figure 1 shows the study area, which includes headwater basins in the Andes Mountains

127   of central Chile and Argentina, between 27 ° S and 38 ° S. These basins supply fresh

128   water to low valleys located on both sides of the Cordillera, a topographic barrier more

129   than 5 km high which strongly controls the spatial variability in atmospheric processes

130   (Garreaud, 2009; Montgomery et al., 2001). In Chile, runoff from the Andes Mountains

131   benefits 75% of the population (http://www.ine.cl) as well as most of the country's

132   agricultural output, hydropower and industrial activities. In the case of Argentina, 7% of

133   the population is located in the provinces of La Rioja, San Juan, Mendoza and northern

134   Neuquén (http://www.indec.gov.ar/), with primary water uses in agriculture and

135   hydropower. The selected watersheds have unimpeded streamflow observations and a

136   snow-dominated hydrologic regime (Figure 2). River basins included in this study have

137   been grouped in eight clusters, or hydrologic response units, based on the seasonality of

138   river flow; numbered C1 to C8 in Figure 1b. Due to differences in topography and

139   locations of stream gages, the number of headwater basins contained within clusters

140   differs markedly on both sides of the Cordillera, with larger watersheds on the

141   Argentinean side.

142   The hydro-climate is mostly controlled by orographic effects on precipitation (Falvey

143   and Garreaud, 2007) and inter-annual variability associated with the Pacific Ocean

144   through the El Niño-Southern Oscillation and Pacific Decadal Oscillation (Masiokas et

145   al., 2006; Newman et al., 2003; Rubio-Álvarez and McPhee, 2010). Precipitation is

146   concentrated in winter months on the western slope (Aceituno, 1988) and sporadic

147   spring and summer storms occur on the mountain front plains of the eastern slope. The

148   vegetation cover presents a steppe type condition on the west slope up to 33 ° S,

149   transitioning to the south into tall bushes and sparse mountain forest. On the eastern

150   slope the steppe vegetation prevails until 37 ° S with an intermittent presence of

151   mountain forests in the Patagonian plains (Eva et al., 2004).

152   Figure 2 summarizes the dominant climatology and associated hydrological regime of

153   rivers in the study region. The temperature seasonality (upper left) is typical of a

154 temperate, Mediterranean climate, and precipitation is strongly concentrated in the fall-

155 winter months of May through August (upper right). The hydrological regime is

156 markedly snow-dominated in the northern part of the domain, which can be seen from

157 the sharp increase in river flow from October and into the summer months of Dec, Jan

158 and Feb (lower right) that follows the seasonal melt of snow (lower left). Only rivers in

159 the southern subregion display a significant rainfall-dominated seasonal hydrograph.

160 The importance of SWE for the region is demonstrated by the fact that for the studied

161 basins, ablation-season (September - March) river flow accounts for two-thirds of

162 average annual streamflow. Maximum SWE accumulation is reached between the

163 months of August and September on the western side and between late September and

164 early October on the eastern side (Figure S4). Scattered snow showers in mid spring

165 (September through November) affect the study area, but they do not affect significantly

166 the decreasing trend of snow-covered area during the melt season (see timing of peak

167 SWE and fractional Snow Covered Area (fSCA) analysis in online supplementary

168 material). This feature is essential for choosing the SWE reconstruction methodology

169 used in this work, which is most applicable to snow regimes with distinct snow

170 accumulation and snow ablation seasons.

171 By and large, the existing network of high-elevation meteorological stations does not

172 include appropriately shielded solid precipitation sensors. Some climate reanalysis

173 products exist, but their representation of Andean topography is crude, and their spatial

174 resolution is not readily amenable to hydrological applications without significant bias

175 correction (Krogh et al., 2015; Scheel et al., 2011). Previous attempts at estimating

176 precipitation amounts at high elevation reaches in the Andes suggest uncertainties on

177 the order of 50% (Castro et al., 2014; Falvey and Garreaud, 2007; Favier et al., 2009).

178 In some basins, runoff is partially dictated by glacier contributions, which occur in

179   summer. According to the Randolph Glacier Inventory (http://www.glims.org/RGI/) the

180   central Andes cordillera has a glacier area of 2,245 km^2 between 27 ° S and 38 ° S,

181   which is equivalent to 1.5% of the modeling domain surface area (~152,000 km^2).

182

183   **3   Methods**

184   **3.1   SWE reconstruction model**

185   A retrospective SWE reconstruction model based on the convolution of the fSCA

186   depletion curve and time-variant energy inputs for each domain pixel is implemented.

187   For each year, the model is run at a daily time step between Aug 15 (end of winter) and

188   Jan 15 (mid-summer). This time window ensures capturing the most likely time at

189   which peak SWE occurs –which itself is variable from year to year- and the almost

190   complete depletion of the seasonal snowpack. Isolated pixels with non-negative fSCA

191   values may remain after Jan 15 at glacier and perennial snowpack sites. However, the

192   relative area that these pixels represent with respect to the entire model domain is very

193   low (< 1.5%), and can be neglected in the context of this work.

194   The energy balance model adopted here derives from the formulation proposed by

195   Brubaker et al. (1996), which considers explicit net shortwave and longwave radiation

196   terms and a conceptual, pseudo-physically based formulation for turbulent fluxes that

197   depends only on the degree-day air temperature:

$$M_p = max\{(Q_{nsw} + Q_{nlw})\, f_B + T_d a_r\,, 0\} \qquad \textbf{[1]}$$

198   Were M_p is potential melt; Q_{nsw} is the net shortwave energy flux; Q_{nlw} is the net

199   longwave energy flux; T_d is the degree-day temperature, a_r [mm °C^{-1} day^{-1}] is the

200   restricted degree-day factor, and f_B is the energy-to-mass conversion factor with a value

201   of 0.26 [mm W^{-1} m^2 day^{-1}]. Actual melt is obtained by multiplying potential melt by

202   fractional snow cover area:

$$M = M_p \, fSCA^{fc} \qquad\qquad \textbf{[2]}$$

203   where $fSCA^{fc}$ is the fSCA MOD10A1 estimate adjusted to forest cover correction by a

204   vegetation fractional f_{veg} (0 to 1) from the MOD44B product (Hansen et al., 2003):

$$fSCA^{fc} = \frac{fSCA^{obs}}{\left(1 - f_{veg}\right)} \qquad\qquad \textbf{[3]}$$

205   The SWE for each pixel is computed for each year by accumulating the melt fluxes

206   back in time during the melt season, starting from the day in which fSCA reaches a

207   minimum value, and up to a date such that winter fSCA has plateaued, according to the

208   relations:

$$SWE_t = SWE_0 - \sum_{1}^{t} M = M_{t+1} + SWE_{t+1} \qquad\qquad \textbf{[4]}$$

$$SWE_0 = \sum_{t=1}^{n} M_t \quad ; \quad SWE_n = 0 \qquad\qquad \textbf{[5]}$$

209   where SWE_0 is end-of-winter or initial maximum SWE accumulation, SWE_n is a

210   minimum or threshold value. The model was run retrospectively until Aug 15, an

211   adequate date before which little melt can be expected for most of the winter seasons

212   within the modeling period in this region (please see Fig. S5 in the online

213   supplementary material).

214   **3.2   Fractional Snow Covered Area and land use data**

215   Spatio-temporal evolution of snow covered area was estimated using the fSCA product

216   from the Moderate Resolution Imaging Spectroradiometer (MODIS) on-board the Terra

217   satellite (MOD10A1 C5 Level 3). The MOD10A1 product provides daily fSCA

218   estimates at 500-m resolution. Percentages of snow extent (i.e. 0% to 100%) are derived

219   from an empirical linearization of the Normalized Difference Snow Index (NDSI),

220   considering the total MODIS reflectance in the visible range (0.545 - 0.565 μm; band 4)

221   and shortwave infrared (1.628 - 1.652 μm; band 6) (Hall et al., 2002; Hall and Riggs,

222   2007).

223   Binary and fractional MODIS fSCA estimates are limited by the use of an empirical

224   NDSI-based method. These errors are notoriously sensitive to surface features such as

225   fractional vegetation and surface temperature (Rittger et al., 2013). Arsenault et al.

226   (2014) reviewed MODIS fSCA accuracy estimates from several studies under different

227   climatic conditions, and report a range between 1.5% and 33% in terms of absolute

228   error with respect to ground observations and operational snow cover datasets. Errors

229   stem mainly from cloud masking and detection of very thin snow (<10 mm depth),

230   forest cover and terrain complexity. In general, commission and omission errors are

231   greatest in the early and late portions of the snow cover season (Hall and Riggs, 2007)

232   and decrease with increasing elevation (Arsenault et al., 2014). Molotch and Margulis

233   (2008) compared MODIS and Landsat Enhanced Thematic Mapper performance in the

234   context of SWE reconstruction, showing that significant differences in SWE estimates

235   were a result of SCA estimation accuracy and less so of model spatial resolution. The

236   latter conclusion supports the feasibility of using the snow covered area products at a

237   500 m spatial resolution for regional scale studies. In order to minimize the effect of

238   cloud cover on the temporal continuity and extent of the fSCA estimates, the

239   MOD10A1 fSCA product was post-processed by a modified algorithm for non-binary

240   products, based on the algorithm proposed by Gafurov and Bárdossy (2009). Their

241   method is adapted here to the fractional snow cover product, applying a three-step

242   correction consisting of: (1) a pixel-specific linear temporal interpolation over 1, 2 or 3

243   days prior and posterior to a cloudy pixel; (2) a spatial interpolation over the eight-pixel

244   kernel surrounding the cloudy pixel, retaining information from lower-elevation pixels

245   only; and (3) assigning the 2001-2014 fSCA pixel specific average when steps (1) and

246 (2) where not feasible. This step minimized the effect of cloud cover on data availability

247 over the spatial domain, yielding cloud cover percentages ranging from21% in

248 September to 8% in December.

249 The Normalized Difference Vegetation Index (NDVI) (Huete et al., 2002) derived from

250 the product MOD13Q1 v5 MODIS Level 3 (16 days - 250 m) is used to classify forest

251 presence for each model pixel. For pixels classified as forested, both fSCA and energy

252 fluxes where corrected: fractional SCA was modified on the basis of percentage forest

253 cover (Molotch, 2009; Rittger et al., 2013), using the average of the forest percentage

254 product from MOD44B V51. Forest attenuation (below canopy) of energy fluxes at the

255 snow surface was estimated from forest cover following the method from Ahl et al.

256 (2006) assuming invariant LAI over each melt season. The selected LAI pattern is

257 obtained by averaging the four LAI scenes available between December - January time

258 window through 14 study years. This time window displays the average state of

259 evergreen forest with the maximum amount of data.

260

261 **3.3   Model forcings**

262 Spatially distributed forcings are required at each grid element in order to run the SWE

263 reconstruction model. In order to ensure the tractability of the extrapolation process, we

264 divided the model domain into sub-regions or clusters, composed by one or more river

265 basins. The river basins were grouped using a clusterization algorithm (please see

266 section S2 on the online supplementary material) based on melt season river flow

267 volume as described in Rubio-Álvarez and McPhee (2010). Then, spatially distributed

268 variables (surface temperature, fSCA, global irradiance) are combined with

269 homogeneous variables for each cluster (e.g. cloud cover index) and point data from

270 meteorological stations in order to obtain a distributed product as described below. A

271   further benefit of the clustering process is that it allows us to analyze distinct regional

272   features of the SWE reconstruction parameters, input variables and output estimates.

273   Net shortwave radiation, Q_{nsw} is estimated as a function of incoming solar radiation

274   based on the equation:

$$Q_{nsw} = (1 - \alpha_s)(G_\downarrow)\tau_a \qquad [6]$$

275   where α_s is snow surface broadband albedo; $G_\downarrow$ is incoming solar radiation (global

276   irradiance); τ_a is the shortwave transmissivity as a function of LAI for mixed forest

277   cover (Pontailler et al., 2003; Sicart et al., 2004), which in turn is estimated as:

$$\tau_a = e^{(-\kappa\,LAI)} \quad ; \quad LAI = -1.323\,ln\left(\frac{0.88 - NDVI}{0.72}\right) \qquad [7]$$

278   with κ = 0.52 for mixed forest species (Dewalle and Rango, 2008). Equation 7 is valid

279   for NDVI values between 0.16 and 0.87. Global irradiance under cloudy sky conditions

280   is estimated considering a daily distributed spatial pattern of clear sky irradiance

281    $G_{c\downarrow}$ derived by the *r.sun* GRASS GIS module (Hofierka et al., 2002; Neteler et al., 2012)

282   and the clear sky index K_c derived from the insolation incident on a horizontal surface

283   from the "Climatology Resource for Agroclimatology" project in the NASA Prediction

284   Worldwide Energy Resource "POWER" (http://power.larc.nasa.gov/) 1°x1° gridded

285   product.

$$G_\downarrow = K_c G_{c\downarrow} \quad ; \quad K_c = \left(\overline{G_{r\downarrow}} / \overline{G_{c\downarrow}}\right) \qquad [8]$$

286   In Equation 8, $\overline{G_{r\downarrow}}$ and $\overline{G_{c\downarrow}}$ are spatial averages over each hydrologic response unit

287   (cluster) of the POWER and *r.sun*-derived products, respectively.

288   A snow-age decay function based on snowfall detection is implemented to estimate

289   daily snow surface albedo (Molotch and Bales, 2006) constrained between values of

290   0.85 and 0.40 (Army Corps of Engineers - USACE, 1960). Snowfall events were

291   diagnosed using a unique minimum threshold for fSCA increments of 2.5% for each

292   hydrologic unit area.

293   Net long wave radiation estimates are derived using:

$$Q_{nlw} = L_{\downarrow}f_{sv}\varepsilon_s + \sigma T_a^4(1 - f_{sv})\varepsilon_{sf} - \sigma T_s^4\varepsilon_s \qquad \textbf{[9]}$$

$$L_{\downarrow} = 0.575\ e_a^{1/7}\sigma T_a^4\ (1 + a_cC^2) \qquad \textbf{[10]}$$

294   Where T_a is air temperature, T_s is the snow surface temperature, ε_s is the snow

295   emissivity (i.e. 0.97), ε_{sf} is the canopy emissivity (i.e. 0.97), f_{sv} is the sky-view factor

296   (i.e. assumed equal to shortwave transmissivity; Pomeroy et al., 2009; Sicart et al.,

297   2004), σ is the Stefan-Boltzmann constant, and $L_{\downarrow}$ is the incoming long wave radiation.

298   Air vapor pressure (e_a) required for long wave radiation estimates was derived from air

299   temperature and relative humidity, which in turn was assumed constant throughout the

300   melt period and equal to 40% based on observations at selected high-elevation

301   meteorological stations. The multiplying factor $(1 + a_cC^2)$ represents an increase in

302   energy input relative to clear sky conditions due to cloud cover, where a_c equals 0.17

303   and $C = 1 - K_c$ is an estimate of the cloud cover fraction (DeWalle and Rango, 2008).

304   Spatially distributed air temperature is generated by combining daily air temperature

305   recorded at index meteorological stations and a weekly spatial pattern of skin

306   temperature derived from the MODIS Land Surface Temperature product

307   (MOD11A1.V5) (Wan et al., 2004; Wan et al., 2002). The product MOD11A1 V5

308   Level 3 estimates surface temperature from thermal infrared brightness temperatures

309   under clear sky conditions using daytime and nighttime scenes and has been shown to

310   adequately represent measurements at meteorological stations ($R^2 \geq 0.7$), displaying

311   moderate overestimation in spring and underestimation in fall (Neteler, 2010). Other

312   studies have reported similar accuracies, with RSME values around 4.5 ºK in cold

313   mountain environments (Williamson et al., 2014). Taking into account the high

314   correlation between air temperature and LST (Benali et al., 2012; Colombi et al., 2007;

315   Williamson et al., 2014), we define:

$$T_a = T_{a\,base} + \Delta T_a = T_{a\,base} + \mu\,(LST - LST_{base}) + \nu \qquad \textbf{[11]}$$

316   were $T_{a\,base}$ is daily air temperature at an index station for each cluster and ΔT_a is the

317   difference in air temperature between any pixel and the pixel where the index station is

318   located. To determine ΔT_a we use a linear regression between MODIS LST data and

319   ΔT_a considering pairs of stations located at high altitude and valley (base) sites, taking

320   into account the melt season average values over the 2001-2014 period. In equation 11,

321    $LST - LST_{base}$ denotes the difference between skin temperatures from any pixel and the

322   index station pixel. The linear regression between skin temperature and air temperature

323   differences has a slope μ of 0.65, an intersect ν of -0.5 and R^2 of 0.93 (Figure S3 in

324   online supplementary material). Estimation of LST during cloudy conditions is done as

325   follows: (1) a pixel-specific linear temporal interpolation is performed over 1 and 2 days

326   prior and posterior to the cloudy pixel; and (2) estimation of remaining null values by

327   an LST-elevation linear regression (Rhee and Im, 2014).

328   This spatial extrapolation method was preferred over more traditional methods -for

329   example based on vertical lapse-rates (Minder et al., 2010; Molotch and Margulis,

330   2008)- after initial tests showed that the combined effect of the relatively low elevation

331   of index stations and the large vertical range of the study domain resulted in

332   unreasonably low air temperatures at pixels with the highest elevations. Likewise, the

333   scarcity of high-elevation meteorological stations and the large spatial extent of the

334   model domain precluded us from adopting more sophisticated temperature estimation

335   methods (e.g. Ragettli et al., 2014).

336   Snow surface temperature and degree-day temperature are estimated (Brubaker et al.,

337   1996) as:

$$T_d = max(T_a, 0) \;\; ; \;\; T_s = min(T_a - \Delta_T, 0) \tag{12}$$

338   where Δ_T is the difference between air and snow surface temperature. To the best of our

339   knowledge, no direct, systematic values of snow surface temperature exist in this

340   region, so for the purposes of this paper we adopt an average value $\Delta_T = 2.5$ [°C],

341   following the suggestion in Brubaker et al., (1996). Slightly higher values ranging from

342   3 to 6°C are shown for continental and alpine snow types (Raleigh et al., 2013)

343   indicating an additional source of uncertainty over net long wave radiation

344   computations. More sophisticated parametrizations for T_s , for example based on heat

345   flow through the snowpack, have been proposed (e.g. Rankinen et al., 2004; Tarboton

346   and Luce, 1996) but those require explicit knowledge about the snowpack temperature

347   profile and/or more complex model formulations to estimate the internal snowpack heat

348   and mass budgets simultaneously.

349   The a_r coefficient in the restricted degree-day energy balance equation was computed

350   using a combination of station and reanalysis data, and assumed spatially homogeneous

351   within each of the clusters that subdivide the model domain. Brubaker et al. (1996)

352   propose a scheme in which this parameter can be explicitly computed from air and snow

353   surface temperature, air relative humidity, and atmospheric pressure and wind speed.

354   Wind speed was obtained from the NASA POWER reanalysis described previously. A

355   correction for atmospheric stability is applied on the bulk transfer coefficient C_h

356   according to the formulation presented by Kustas et al. (1994), assuming a surface

357   roughness of 0.0005 m:

$$C_h = \begin{cases} (1 - 58R_i)^{0.25} \; for \; R_i < 0 \\ (1 + 7R_i)^{-0.1} \; for \; R_i > 0 \end{cases} \quad ; \quad R_i = \frac{gz(T_a - T_s)}{u^2 T_a} \qquad \text{[13]}$$

358   Where R_i is the Richardson number, g is the gravity acceleration (9.8 [m s^{-2}]), z is the

359   standard air temperature measurement height (2 m) and u is wind speed. The

360   calculation of R_i and a_r is based on the standard assumptions of T_s at the freezing point

361   and a water vapor saturated snow surface over all high-elevation meteorological stations

362   with available air temperature and relative humidity records (Molotch and Margulis,

363   2008). Further in the text, we discuss some implications of these assumptions and of the

364   input data used on the ability of the model of simulating relevant components of the

365   snowpack energy exchange.

366   Table 1 shows the main cluster characteristics and regionalized model parameters. It can

367   be seen that for those clusters located in the southern and middle reaches of the model

368   domain, the a_r parameter values range from 0.10 to 0.23 [cm °C^{-1} day^{-1}], which is

369   similar to values reported in previous studies performed in other mountain ranges in the

370   Northern Hemisphere (0.20 − 0.25 in Martinec (1989), 0.17 in Kustas et al., (1994),

371   0.20 in Brubaker at al., (1996), 0.15 in Molotch and Margulis (2008)). However, values

372   associated to the northernmost clusters of our study area are quite low, reaching under

373   0.02 for the C1 cluster in northern Chile.

374   Clear sky index (K_C) values range between 0.78 and 0.89 which is similar to values

375   reported by Salazar and Raichijk (2014) who estimate K_c values on the order of 0.90 for

376   a single location at 1200 m.a.s.l. in northern Argentina. A 5 to 6 °C difference can be

377   observed in mean air temperature at index stations between the northern and southern

378   edge of the domain. Temperatures for the C4 cluster are subject to greater uncertainty,

379   because no high-elevation climate station data was available for this study (Figure S4).

380   Forest cover values are lower than 6% throughout the model domain, with the exception

381 of cluster C3, with a value of 13.8%. The difference in forest cover between clusters C3

382 and C8 can be attributed to the precipitation shadow effect induced by the Andes ridge.

383 Forest corrections applied to MODIS fSCA resulted in a 17% increase with respect to

384 the original values over the southern sub-domain (C3).

385 **3.4   Evaluation data: SWE, snow depth and river flow observations**

386 Operational daily snow-pillow data from stations maintained by government agencies in

387 Chile and Argentina were available for this study (Table 2). Only stations with ten or

388 more years of record were included and manual snow course data were neglected

389 because of their discontinuous nature. Approximately 10% of observed maximum SWE

390 accumulation values were discarded due to obvious measurement errors and data gaps.

391 An analysis of the seasonal variability of snow-pillow records on the western and

392 eastern slopes of the Andes suggests that peak-SWE date is somewhat delayed on the

393 latter, by approximately one month. Therefore, peak-SWE estimates for Chilean and

394 Argentinean stations are evaluated on September 1 and October 1, respectively,

395 although in the results section we show values for September 15 in order to use a unique

396 date for the entire domain. Manual snow depth observations were taken in the vicinity

397 of selected snow-pillow locations in order to evaluate the representativeness of these

398 measurements at the MODIS grid scale during the peak-SWE time window. These

399 depth observations were obtained in regular grid patterns within an area the

400 approximate size of a MODIS pixel (500 m), centered about the snow-pillow location.

401 On average, 120 depth observations spaced at approximately 50-m increments were

402 obtained at each snow pillow site. Snow density was estimated by a depth-weighted

403 average of snow densities measured in snow pits with a 1000-cc snow cutter. Samples

404 where obtained either at regular 10-cm depth intervals along the snow pit face, or at the

405 approximate mid depth of identifiable snow strata for very shallow snow pack

406 conditions. Weights were computed as the fraction of total depth represented by each

407 snow sample.

408 Distributed snow depth observations were available from snow surveys carried out

409 during late winter between 2010 and 2014 at seven study catchments in the western side

410 of the Andes, between latitudes 30 ° S and 37 ° S (Figure1, Table 3). Snow depths were

411 recorded with 3 m graduated avalanche probes inserted vertically into the snow pack.

412 Depending on the terrain conditions, between three and five individual point snow depth

413 measurements were obtained at each location, from which a mean snow depth and

414 standard error are calculated; i.e. three-point observations are made forming a line with

415 a spacing of one meter and five-point observations are made forming a cross with an

416 angle of 90 degrees and a spacing of one meter. Pixel-scale SWE estimates are obtained

417 by averaging all depth observations within the limits of MODIS pixels and multiplying

418 them by density observations from snow pits excavated at the time of each snow survey;

419 i.e. two or three snow pits per field campaign. After this, individual depth observations

420 are converted into SWE for model validation. Modeled SWE values are averaged at all

421 MODIS pixels where manual depth observations are available, and their summary

422 statistics are compared to those of SWE estimated from manual depth observations at

423 the same pixels, multiplied by average density from snow pits.

424 Spring and summer season (September to March) total river flow volume (SSRV) for

425 the 2001-2014 period are obtained from unimpaired (no human extractions) streamflow

426 records at river gauges located in the mountain front along the model domain. Data

427 were pre-selected leaving out series that showed too many missing values, and verified

428 through the double mass curve method (Searcy and Hardison, 1960) in order to discard

429 anomalous values and to ensure homogeneity throughout the period of study. Regional

430 consistency was verified through regression analysis, only including streamflow records

431 with R^2 values greater than 0.5 among neighboring catchments. Missing values

432 constituted about 3.7% of the entire period and were filled through linear regression.

433

434 **4   Results**

435 **4.1   Model validation**

436 Figure 3 compares reconstructed peak SWE (gray circles) to observed values at three

437 snow-pillow locations (black diamonds) where additional validation sampling at the

438 MODIS pixel scale was conducted (box plots). At the Cerro Vega Negra site (CVN),

439 located in cluster C1, the model overestimates peak SWE (September 1) with respect to

440 the snow-pillow value by 97% in 2013 and by 198% in 2014. At the Portillo site (POR,

441 cluster C2), reconstructed SWE underestimates recorded values by 51% in 2013 and

442 72% 2014. At the Laguna Negra site (LAG, also C2), reconstructed peak SWE slightly

443 overestimates recorded values (8%) (Table 4). However, reconstructed SWE compares

444 favorably to distributed manual SWE observations obtained in the vicinity of the snow

445 pillows at the POR and LAG sites. At POR, model estimates approach upper (2012) and

446 lower (2013 and 2104) quartiles, while at LAG the model estimates are closer to the

447 minimum value observed in 2013 and very similar to the observed mean in 2014.

448 Figure 4 depicts the comparison between reconstructed SWE and snow surveys carried

449 out at pilot basins throughout the model domain. From left to right, it can be seen that

450 the model slightly overestimates SWE with respect to observations at CVN (i.e. 18%

451 overestimation). Further south, there is a very good agreement at ODA - MAR (i.e. 4%

452 underestimation), with less favorable results at MOR - LVD (i.e. 39% underestimation)

453 and OB - RBL (i.e. 36% underestimation). At CHI the model significantly

454 underestimates SWE (i.e. by 67%); note this site is heavily forested. For the 2013a and

455 2014a boxes (Figure 4) –which correspond to clearing sites-, there is still

456 underestimation, but of lesser magnitude (20%). Summarizing, we detect model

457 overestimation respect to snow survey medians in four cases and underestimation in

458 fifteen cases. In 11 out of 19 cases, reconstructed SWE lies within the snow survey data

459 uncertainty bounds (standard deviation).

460 Figure 5 shows a comparison between model estimates of peak (Sep 15th) SWE and

461 corresponding observations at snow pillow sites. In general, directly contrasting pixel-

462 based estimates with sensor observations should be attempted with caution. In areas

463 with complex topography, slight variations in the position of the sensor with respect to

464 the model grid, combined with high spatial variability in snow accumulation could lead

465 to large differences between model estimates and observations. Also, small-scale

466 variations in snow accumulation near the sensor, for example induced by protective

467 fences, could introduce bias to the results (e.g. Meromy et al., 2013; Molotch and Bales,

468 2006; Rice and Bales, 2010). Taking the above into consideration, Figure 5 suggests

469 that the model tends to overestimate observed peak SWE at the two northernmost sites

470 on the Chilean side (QUE and CVN); the equivalent cluster on the Argentinean side

471 (C4) lacks SWE observations. The R^2 values indicated below refer to the best linear fit;

472 regression line slope and intercept coefficients are provided in Table 4. Overall, we find

473 a better agreement at the eastern slope sites (i.e. $R^2 = 0.74$) than at their western

474 counterparts (i.e. $R^2 = 0.43$), with a combined R^2 value of 0.61. Individually, the worst

475 and best linear agreements are obtained at POR ($R^2=0.32$) and LOA ($R^2=0.88$),

476 respectively. Time series of observed SWE and model estimates for these two extreme

477 cases are shown in the supplementary online material, and indicate a significant degree

478 of inter-annual variability in model discrepancies in terms of peak SWE, but less in

479 terms of, for instance, snow cover duration. Average standard error, $SE_{\bar{x}}$ is 284 mm

480 ($SE_{\bar{x}}$ =242 mm at the west slope; $SE_{\bar{x}}$=302 mm at the east slope), with a range between

481 72 mm (TOS) and 378 mm (ATU) (Table 4). Relative errors display some variability,

482 with overestimation higher than 30% at the two northernmost (QUE and CVN) and at

483 the southernmost (PEH) snow pillows. For all other snow pillows, the model estimates

484 are lower than the sensor observation; the range of relative errors for those sites with

485 underestimation goes from -52% to -5%.

486 **4.2   Correlation with melt-season river flows**

487 Under the assumption of unimpaired flows, peak SWE and seasonal flow volume

488 should show some degree of correlation, even though no assumptions can be made here

489 about other relevant hydrologic processes, such as flow contributions from glaciated

490 areas, subsurface storage carryover at the basin scale and influence of spring and

491 summer precipitation. Differences can be expected due to losses to evapotranspiration

492 and sublimation affecting the snowpack and soil water throughout the melt season.

493 Hence, basin-averaged peak SWE should always be higher than melt season river

494 volume. A clear regional pattern emerges when inspecting the results of this comparison

495 in Figure 6. Correlation between peak SWE and melt season river flow is higher in

496 clusters C1 and C4 with R^2 values of 0.84 and 0.86, respectively. The result for Cluster

497 C4 indicates that liquid precipitation during the melt season (Figure 2) does not result in

498 decreased correlation between peak SWE and river flow. Clusters C2, C5, C6 and C7

499 display a somewhat lower correlation, with some individual years departing more

500 significantly from the overall linear trend. R^2 values range between 0.46 and 0.78 in

501 these cases. Finally, not only are correlation coefficients lower for the southern clusters

502 C3 ($R^2 = 0.56$) and C8 ($R^2 = 0.48$), but also estimated peak SWE is always lower than

503 river flow, which indicates the importance of spring and summer precipitation in

504 determining streamflow variability. In fact, Castro et al. (2014) analyze patterns of daily

505 precipitation in this area and document average spring and summer rainfall amounts of

506 approximately 520 mm in C3 and 85 mm in C8. A promising avenue for further

507 research in this region emerges when comparing the correlation between melt-season

508 river flow and the spatially distributed reconstructed product versus that of river flows

509 and snow pillow data. Table 5 shows values of R^2 for the linear regression between

510 these variables. It can be seen that for two of the three clusters on the western side of the

511 continental divide, the end-of-winter distributed reconstruction has more predictive

512 power than observed SWE. Only for central Chile the *Laguna Negra* (LAG, with a

513 value of 0.82) site has a better correlation with river flows, but the reconstructed

514 product has a value of 0.78, which lies in between those found for LAG and for *Portillo*

515 (POR, with a value of 0.68). For the eastern side of the continental divide, the

516 distributed product shows similar skill than that of snow pillows except for Atuel, which

517 has a very high correlation (R^2 of 0.87) with cluster C6 river flows, and for cluster C7,

518 in which the reconstruction shows higher predictive power (R^2 of 0.89) than the

519 available SWE observations (VAL and PEH).

520

521 **4.3   Regional SWE estimates**

522 Figure 7 shows the Sep 15 SWE average over the 2001 – 2014 period obtained from the

523 reconstruction model, and the percent annual deviations (anomalies) from that average.

524 Steep elevation gradients can be inferred from the climatology, as well as the latitudinal

525 variation expected from precipitation spatial patterns. For the northern clusters (C1 and

526 C4), the peak SWE averaged over snow covered areas is on the order of 300 mm while

527 in the middle of the domain (C2, C5, C6), it averages approximately 750 mm. The

528 southern clusters (C3, C7, C8) do show high accumulation averages (approximately 650

529 mm), despite the sharp decrease in the Andes elevation south of latitude 34 º S. The

530 anomaly maps convey the important degree of inter-annual variability, as well as

531 distinct spatial patterns associated with it. Between 2001 and 2014, years 2002 and

532 2005 stand out for displaying large positive anomalies throughout the entire

533 mountainous region of the model domain, with values 2000 mm and more above the

534 simulation period average. Other years prior to 2010 show differential accumulation

535 patterns, where either the northern or southern parts of the domain are more strongly

536 affected by positive or negative anomalies. Overall, the northern clusters (C1 and C4)

537 show above-average accumulation in only three (2002, 2005 and 2007) of the 14

538 simulated years, whereas the other clusters show above-average accumulation for six

539 years (2001, 2002, 2005, 2006, 2008 and 2009). In particular, years 2007 and 2009

540 show a bimodal spatial structure, with excess accumulation (deficit) in the northern

541 (southern) clusters during the former, and the inverse pattern in the latter year.

542 A longitudinal pattern in the distribution of negative anomalies can be discerned from

543 Figure 7, whereby drought conditions tend to be more acute on one side of the divide

544 versus the other. Conversely, during positive anomaly years, both sides of the Andes

545 seem to show similar behavior. Further research on the mechanisms of moisture

546 transport during below-average precipitation years may shed light on this result.

547 Figure 8 provides a different perspective on the region's peak SWE climatology by

548 presenting our results aggregated into elevation bands for each hydrologic unit.

549 Elevation bands are defined at 1000-m increments starting from 1000 m.a.s.l. Crosses

550 indicate average peak SWE for each band (mm), and circle areas are proportional to the

551 surface area covered by each elevation band. From north to south, hydrologic unit C4

552 shows slightly higher SWE than C1 between 3000 and 5000 m.a.s.l.., but much larger

553 surface areas (~32,000 vs. ~17,000 km2), indicating a larger water resource potential.

554 C2 stands out as having the greatest area-weighted cluster SWE and the greatest SWE

555 for each elevation band. Compared to its counterpart on the eastern side of the Andes

556   range (C5), C2 shows higher accumulations (up to ~1800 mm) at all elevations. The

557   area included between 2000 and 4000 m.a.s.l. (~13,000 km2), which shows an

558   estimated peak SWE accumulation on the order of 600 mm, represents the most

559   predominant snow volume accumulation zone. Although the 4000-5000 m.a.s.l.

560   elevation band contributes approximately half the 2000 - 4000 band surface area in C2,

561   its average peak SWE is roughly twice that of the 3000-4000 band (~6,000 km2). This

562   makes this subregion interesting for future research, because most snow observations in

563   the area are obtained below 4000 m.a.s.l.; the same is true for unit C5. Further to the

564   south, the barrier effect of the Andes is also suggested by the displacement of the SWE-

565   elevation distribution in C6 and C7 when compared to C3. On the eastern side of the

566   model domain, it is interesting to see a steepening of the average peak SWE elevation

567   profile between C6 and C8, suggesting that C8 is less affected by Andes blockage than

568   its northern counterparts.

569   Estimated net energy inputs (Figure 9) shows a decrease from the northern (C1 and C4)

570   into the mid-range clusters (C2, C5 and C6), with increases again in the southern

571   reaches of the domain (C3, C7 and C8). This is a result of a combination of an

572   increasing trend in net shortwave radiation in the south-north direction and a reverse

573   spatial trend in net long wave radiation exchange, which increases (approaches less-

574   negative values) in the north-south direction. Modeled turbulent energy fluxes

575   (Equation 1) are negligible in the northern clusters, but their contribution to the net

576   energy exchange increases with latitude as a result of the spatial variation in the a_r

577   parameter.

578   Figure 10 shows the temporal (seasonal) variation in average fSCA and SWE for each
579   cluster, and

580 **Table 5. Coefficient of determination R^2 between river melt season flows (SSRV), estimated and**
581 **observed SWE (end-of-winter).**

582

	R2 values specific SSRV vs. Estimated SWE per cluster		R2 values specific SSRV vs. SWE at snow pillows (2001 – 2013)*	
	2001 - 2014	Neglecting 2009 at Argentinean clusters**	Best	2nd best
c1	0.84	***	0.74 (CVN)	0.69 (QUE)
c2	0.78	***	0.82 (LAG)	0.68 (POR)
c3	0.57	***	0.17 (LOA)	0.16 (ALT)
c4	0.87	***	***	-
c5	0.66	0.82	0.81 (TOS)	-
c6	0.45	0.76	0.87 (ATU)	0.77 (DIA)
c7	0.64	0.89	0.77 (VAL)	0.41 (PEH)
c8	0.48	0.64	***	-

583 *** 2014 flows in Argentina unavailable to us at the moment of writing.**
584 **** 2009 is considered an outlier year for the reconstruction at Argentinean sites.**
585

586 **Table 6. Peak SWE 2001 - 2014 climatology for river basins within the study region. Basin-wide**
587 **averages, SCA-wide averages and basin-wide water volumes shown**

588   shows peak SWE at the watershed scale, averaged both over the entire basin and over

589 the snow covered area. Maximum fSCA increases in the north-south direction,

590 consistently with the climatological increase in winter precipitation and decrease in

591 temperature. A dramatic increase in snow coverage is observed between the northern

592 (i.e. C1 and C4) and adjacent southern clusters (i.e. C2 and C5), with average peak

593 fSCA increasing from 20% to 50%. The highest average snow coverage is observed for

594 cluster C8, with more than 60%. Snow water equivalent displays a similar regional

595 variability with lower seasonal variability than snow cover for all clusters except for C2,

596 where fSCA and SWE variability throughout the melt season are identical. Mean peak

597 SWE in northern Chile is the lowest among the eight clusters, with approximately 100

598 mm SWE over the 2001-2014 period. The largest estimate is for cluster C2, central

599 Chile, where mean peak SWE exceeds 500 mm. The rain shadow effect of the Andes

600 range is apparent in the comparison of SWE and fSCA in C2 and C5-C6-C7. Fractional

601 snow covered area is lower on the east side because of the larger basin sizes which

602 increases the proportional area of lower elevation terrain. In addition, peak SWE is

603 approximately 25% lower on the east side, with less than 400 mm SWE for the eastern

604 clusters. Cluster C4 is not affected by this phenomenon, showing higher snow coverage

605 and water equivalent accumulation than its counterpart, C1. Cluster C8 represents an

606 interesting exception in that its average fSCA is the largest within the model domain,

607 but peak SWE is not significantly higher than the estimates in the other clusters on the

608 Argentinean side of the Andes.

609

610 **5   Discussion**

611 **5.1   Sensitivity analysis**

612 The Andes cordillera, on one hand, displays ideal conditions for SWE reconstruction,

613 including low cloud cover, infrequent snowfall during spring and summer, and very low

614 forest cover. On the other hand, the scarcity of basic climate data poses challenges that

615 would affect any modeling exercise. A local sensitivity analysis is implemented in order

616 to gain insights regarding the influence of some of the assumptions required for SWE

617 modeling (Figure 11). The influence of the clear sky factor (Kc), snow surface albedo

618 ($\propto_s$), the slope of the Δ_{LST} vs. Δ_{Ta} relationship (μ), the a_r parameter, and the difference

619 between air and snow surface temperature are explored. Results are shown for the

620 model pixels corresponding to two of the snow pillow sites, each located at the northern

621 and southern sub-regions of the model domain respectively. The clear sky factor, snow

622 albedo and Δ_{LST} vs. Δ_{Ta} slope are the most sensitive parameters at the northern (CVN)

623 site. Increasing the slope in the Δ_{LST} vs. Δ_{Ta} relationship results in decreasing

624 temperature at pixels with higher elevations than the index station, thus lowering long

625 wave cooling and resulting in higher SWE estimates. The impact of increasing slope

626 values decreases progressively, because an increasing slope results in increased pixel air

627 temperature, but snow surface temperature cannot exceed 0º C. The influence of snow

628 albedo is analyzed by perturbing the entire albedo time series for each season from the

629 values predicated by the USACE model. Increasing albedo values restricts the energy

630 available for melt therefore decreasing peak SWE estimates. Again, a nonlinear effect is

631 observed, constrained by a minimum albedo value of 0.4. The sensitivity of the clear

632 sky factor, on the other hand, is monotonic, with increasing values generating more

633 available solar energy, resulting in higher SWE estimates. At the southern site (ALT),

634 the shape of the sensitivity functions is the same as at CVN, but the magnitude of SWE

635   variations as a function of parameter perturbations is smaller. This is likely related to

636   the fact that turbulent fluxes constitute a larger fraction of the simulated overall energy

637   balance at the southern sites; a_r parameter values are greater in the southern portions of

638   the domain. Therefore, perturbations of the other terms account for a smaller fraction of

639   the energy exchange at the southern sites.

640   **5.2   Model performance and conceptual energy balance representation**

641   Among the many factors that influence model performance, the sub-region delineation

642   involves the selection of index meteorological stations for extrapolating input data at the

643   domain level. Thus, for example, two adjacent pixels that are part of different sub-

644   regions may be assigned input data derived from two different meteorological stations

645   that are many kilometers apart. It would be preferable to use distributed inputs only, but

646   these were not available for this domain. Future research is needed to explore

647   alternative strategies for domain clustering.

648   Overall, the model performance, evaluated against SWE observations, is comparable to

649   that achieved in other mountain regions of the world. Our average coefficient of

650   determination R^2 of 0.68 is lower than that obtained by Guan et al. (2013) in the Sierra

651   Nevada (0.74) when comparing operational snow pillow observations, although this

652   value is affected by three stations with much lower agreement (POR, LAG, ATU); the

653   median R^2 in our study, on the other hand, is 0.73, which we consider satisfactory in

654   light of the scarcity of forcing data and direct snow properties observations available in

655   this region. The overall relative error is -2% for observations from snow pillows within

656   our study region, but this value is strongly affected by two stations where we observed

657   significant overestimation (QUE and CVN). When including the remaining ten snow

658   pillows only, relative error increases to -16%. Given that forest cover is minimal in our

659   modeling domain, we can attribute this bias to either weaknesses in the simplified

660   energy balance model formulation or to errors in the MOD10A1 fSCA product.

661   Previous work in the northern hemisphere (Rittger et al., 2013) has shown that MODIS

662   can underestimate fractional snow cover during the snowmelt season. On one hand, land

663   cover heterogeneity at spatial resolutions lower than the MODIS scale (i.e. 500 m)

664   result in mixed-pixel detection problems. On the other hand, spectral unmixing based on

665   the NDSI approach tends to underestimate fSCA under patchy snow distributions. In

666   addition, surface temperatures greater than 10 °C –more likely to exist during late

667   spring- induce MODIS fSCA underestimation. Molotch and Margulis (2008) tested the

668   SWE reconstruction model using Landsat ETM and MOD10A1 and found that

669   maximum basin-wide mean SWE estimates were significantly lower when using

670   MOD10A1. More recently, Cortés et al. (2014) showed that a similar pattern can be

671   seen for the extratropical Andes, whereby MODIS fSCA consistently underestimated

672   LANDSAT TM fSCA retrievals. MODIS fSCA underestimation during spring

673   combined with increased net energy fluxes over the snowpack can result in a marked

674   underestimation (~20%) for available energy flux for snowpack melting and

675   consequently (~45%) for maximum SWE (Molotch and Margulis, 2008).

676   Comparisons against spatial interpolations from intensive-study areas in the Sierra

677   Nevada or Rocky Mountains (e.g. Erxleben et al., 2002; Jepsen et al., 2012) are not

678   directly applicable, because in this study we do not employ interpolation methods to

679   derive our manual snow survey SWE estimates. However, the average overestimation

680   found with respect to snow survey data could be explained by the fact that manual

681   surveys are limited by site accessibility and sampling procedures. For example, snow

682   probes utilized are only 3.0 m long, which precludes observation of deeper snowpack;

683   likewise, deep snow is expected in sites exposed to avalanching, which were generally

684   avoided in snow survey design due to safety considerations. On the other hand, manual

685 snow surveys do not visit steep snow-free areas where snow depth is expected to be

686 lower than the 500-m pixel reconstruction. The combined effect of these two contrasting

687 effects is the subject of further research in this region.

688 Another possible explanation for model errors is the simplified formulation of the

689 energy balance equation, which may be problematic when applied over a large,

690 climatically variable model domain. To explore the implications of the simplified

691 energy balance with respect to model errors, we focus on the representation of turbulent

692 energy fluxes, represented here through a linear temperature-dependent term. Figure 12

693 describes the spatial distribution of the a_r parameter, and its dependence on air

694 temperature and relative humidity observed at index meteorological stations. The

695 implication for energy balance modeling is that turbulent fluxes would account for a

696 very small portion of the snowpack energy and mass balance in the northern area (C1

697 and C4), which is characterized by low air temperatures and relative humidity, which

698 yield very low a_r values. The reader must recall that a_r values were computed based on

699 index station data and assumed spatially homogeneous over each cluster. The simplified

700 model formulation used in this research, however, although pseudo-physically based -

701 compared to degree-day or fully calibrated models- allows only for positive net

702 turbulent fluxes, because both the a_r and the degree-day temperature index are positive

703 values. However, previous studies in this region (Corripio and Purves, 2005; Favier et

704 al., 2009) have suggested that latent heat fluxes have a relevant role because of high

705 sublimation rates favored by high winds and low relative humidity conditions

706 predominant in the area.

707 In order to diagnose differential performance of the model across the hydrologic units

708 defined in this study, we compute the Bowen ratio (β) at the point scale from data

709 available only at the few high elevation meteorological stations in the region with

710   recorded relative humidity. The calculations show that at stations located within cluster

711   C1, latent heat fluxes are opposite in sign and larger in magnitude than sensible heat

712   fluxes (Figure S6 in supplementary material). While this results in net turbulent cooling

713   of the snowpack, this energy loss is not considered in our simplified energy balance

714   approach. Note that for the clusters C5, C6, C7 and C8, all located on the eastern

715   (Argentinean) slope of the Andes, sensible and latent heat fluxes are positive, compared

716   to negative latent heat fluxes for all the index stations within clusters C2 and C3 on the

717   Chilean side. This result is consistent with Insel et al. (2010), who applied a Regional

718   Circulation Model (RegCM3) in the area and showed a significant difference in relative

719   humidity (~70% east side vs. ~40% west side). The fact that we extrapolate the a_r

720   parameter value based on relatively low elevation meteorological observations

721   throughout the southern Argentinean hydrologic units may result in a yet not quantified

722   overestimation of seasonal energy inputs and peak SWE for those clusters.

723

724   6   Conclusions

725   Snow water equivalent is the foremost water source for the extratropical Andes region

726   in South America. This paper presents the first high-resolution distributed assessment of

727   this critical resource, combining instrumental records with remotely sensed snow

728   covered area and a physically-based snow energy balance model. Overall errors in

729   estimated peak SWE, when compared with operational station data, amount to -2.2%,

730   and correlation with observed melt-season river flows is high, with an R^2 value of 0.80.

731   MODIS Fractional SCA data proved adequate for the goals of this study, affording high

732   temporal resolution observations and an appropriate spatial resolution given the extent

733   of the study region. These results have implications for evaluating seasonal water

734   supply forecasts, analyzing synoptic-scale drivers of snow accumulation, and validating

735   precipitation estimates from regional climate models. In addition, the strong correlation

736   between peak SWE and seasonal river flow indicates that our results could be useful for

737   the evaluation of alternative water resource projects as part of development and climate

738   change adaptation initiatives. Finally, the regional SWE and anomaly estimates

739   illustrate the dramatic spatial and temporal variability of water resources in the

740   extratropical Andes, and provide a striking visual assessment of the progression of the

741   drought that has affected the region since 2009. These results should motivate further

742   research looking into the climatic drivers of this spatially distributed phenomenon.

749   **Bibliography**

750   Aceituno, P., 1988. On the functioning of the Southern Oscillation in the South

751   American sector. Part I: Surface climate. Mon. Weather Rev. 116, 505–524.

752   Ahl, D.E., Gower, S.T., Burrows, S.N., Shabanov, N.V., Myneni, R.B., Knyazikhin, Y.,

753   2006. Monitoring spring canopy phenology of a deciduous broadleaf forest using

754   MODIS. Remote Sens. Environ. 104, 88–95.

755   Aravena, J.-C., Luckman, B.H., 2009. Spatio-temporal rainfall patterns in southern

756   South America. Int. J. Climatol. 29, 2106–2120.

757   Army Corps of Engineers, U., 1960. Engineering and design: runoff from snowmelt.

758 [publisher not identified], [Washington.

759 Arsenault, K.R., Houser, P.R., De Lannoy, G.J.M., 2014. Evaluation of the MODIS

760 snow cover fraction product. Hydrol. Process. 28, 980–998. doi:10.1002/hyp.9636

761 Ayala, A., McPhee, J., Vargas, X., 2014. Altitudinal gradients, midwinter melt, and

762 wind effects on snow accumulation in semiarid midlatitude Andes under La Niña

763 conditions. Water Resour. Res. 50, 3589–3594. doi:10.1002/2013WR014960

764 Benali, A., Carvalho, A.C., Nunes, J.P., Carvalhais, N., Santos, A., 2012. Estimating air

765 surface temperature in Portugal using MODIS LST data. Remote Sens. Environ. 124,

766 108–121.

767 Brubaker, K., Rango, A., Kustas, W., 1996. Incorporating Radiation Inputs into the

768 Snowmelt Runoff Model. Hydrol. Process. 10, 1329–1343. doi:10.1002/(SICI)1099-

769 1085(199610)10:10<1329::AID-HYP464>3.0.CO;2-W

770 Castro, L.M., Gironás, J., Fernández, B., 2014. Spatial estimation of daily precipitation

771 in regions with complex relief and scarce data using terrain orientation. J. Hydrol. 517,

772 481–492.

773 Cline, D.W., Bales, R.C., Dozier, J., 1998. Estimating the spatial distribution of snow in

774 mountain basins using remote sensing and energy balance modeling. Water Resour.

775 Res. 34, 1275–1285.

776 Colombi, A., De Michele, C., Pepe, M., Rampini, A., 2007. Estimation of daily mean

777 air temperature from MODIS LST in Alpine areas. EARSeL EProceedings 6, 38–46.

778 Corripio, J.G., Purves, R.S., 2005. Surface energy balance of high altitude glaciers in

779 the central Andes: The effect of snow penitentes. Clim. Hydrol. Mt. Areas 15–27.

780 Cortés, G., Cornwell, E., McPhee, J.P., Margulis, S.A., 2014. Snow Cover
781 Quantification in the Central Andes Derived from Multi-Sensor Data, in: AGU Fall
782 Meeting Abstracts. p. 0410.

783 Cortés, G., Girotto, M., Margulis, S.A., 2014. Analysis of sub-pixel snow and ice extent
784 over the extratropical Andes using spectral unmixing of historical Landsat imagery.
785 Remote Sens. Environ. 141, 64–78. doi:10.1016/j.rse.2013.10.023

786 Cortés, G., Vargas, X., McPhee, J., 2011. Climatic sensitivity of streamflow timing in
787 the extratropical western Andes Cordillera. J. Hydrol. 405, 93–109.
788 doi:10.1016/j.jhydrol.2011.05.013

789 DeWalle, D., Rango, A., 2008. Principles of snow hydrology. Cambridge University
790 Press, New York.

791 Dietz, A.J., Kuenzer, C., Gessner, U., Dech, S., 2012. Remote sensing of snow–a
792 review of available methods. Int. J. Remote Sens. 33, 4094–4134.

793 Erxleben, J., Elder, K., Davis, R., 2002. Comparison of spatial interpolation methods for
794 estimating snow distribution in the Colorado Rocky Mountains. Hydrol. Process. 16,
795 3627–3649.

796 Eva, H.D., Belward, A.S., De Miranda, E.E., Di Bella, C.M., Gond, V., Huber, O.,
797 Jones, S., Sgrenzaroli, M., Fritz, S., 2004. A land cover map of South America. Glob.
798 Change Biol. 10, 731–744.

799 Falvey, M., Garreaud, R., 2007. Wintertime precipitation episodes in central Chile:
800 Associated meteorological conditions and orographic influences. J. Hydrometeorol. 8,
801 171–193.

802 Falvey, M., Garreaud, R.D., 2009. Regional cooling in a warming world: Recent

803 temperature trends in the southeast Pacific and along the west coast of subtropical South

804 America (1979–2006). J. Geophys. Res. Atmospheres 114, D04102.

805 doi:10.1029/2008JD010519

806 Favier, V., Falvey, M., Rabatel, A., Praderio, E., López, D., 2009. Interpreting

807 discrepancies between discharge and precipitation in high-altitude area of Chile's Norte

808 Chico region (26–32°S). Water Resour. Res. 45, W02424. doi:10.1029/2008WR006802

809 Gafurov, A., Bárdossy, A., 2009. Cloud removal methodology from MODIS snow

810 cover product. Hydrol. Earth Syst. Sci. 13, 1361–1373.

811 Garreaud, R.D., 2009. The Andes climate and weather. Adv. Geosci. 22, 3–11.

812 Gascoin, S., Lhermitte, S., Kinnard, C., Bortels, K., Liston, G.E., 2013. Wind effects on

813 snow cover in Pascua-Lama, Dry Andes of Chile. Adv. Water Resour. 55, 25–39.

814 doi:10.1016/j.advwatres.2012.11.013

815 Guan, B., Molotch, N.P., Waliser, D.E., Jepsen, S.M., Painter, T.H., Dozier, J., 2013.

816 Snow water equivalent in the Sierra Nevada: Blending snow sensor observations with

817 snowmelt model simulations. Water Resour. Res. 49, 5029–5046.

818 doi:10.1002/wrcr.20387

819 Hall, D.K., Riggs, G.A., 2007. Accuracy assessment of the MODIS snow products.

820 Hydrol. Process. 21, 1534–1547.

821 Hall, D.K., Riggs, G.A., Salomonson, V.V., DiGirolamo, N.E., Bayr, K.J., 2002.

822 MODIS snow-cover products. Remote Sens. Environ. 83, 181–194.

823 Hansen, M.C., DeFries, R.S., Townshend, J.R.G., Carroll, M., Dimiceli, C., Sohlberg,

824   R.A., 2003. Global percent tree cover at a spatial resolution of 500 meters: First results

825   of the MODIS vegetation continuous fields algorithm. Earth Interact. 7, 1–15.

826   Hofierka, J., Suri, M., others, 2002. The solar radiation model for Open source GIS:

827   implementation and applications, in: Proceedings of the Open Source GIS-GRASS

828   Users Conference. pp. 1–19.

829   Huete, A., Didan, K., Miura, T., Rodriguez, E.P., Gao, X., Ferreira, L.G., 2002.

830   Overview of the radiometric and biophysical performance of the MODIS vegetation

831   indices. Remote Sens. Environ. 83, 195–213.

832   Insel, N., Poulsen, C.J., Ehlers, T.A., 2010. Influence of the Andes Mountains on South

833   American moisture transport, convection, and precipitation. Clim. Dyn. 35, 1477–1492.

834   Jepsen, S.M., Molotch, N.P., Williams, M.W., Rittger, K.E., Sickman, J.O., 2012.

835   Interannual variability of snowmelt in the Sierra Nevada and Rocky Mountains, United

836   States: Examples from two alpine watersheds. Water Resour. Res. 48.

837   Krogh, S.A., Pomeroy, J.W., McPhee, J., 2015. Physically Based Mountain

838   Hydrological Modeling Using Reanalysis Data in Patagonia. J. Hydrometeorol. 16,

839   172–193. doi:10.1175/JHM-D-13-0178.1

840   Kustas, W.P., Rango, A., Uijlenhoet, R., 1994. A simple energy budget algorithm for

841   the snowmelt runoff model. Water Resour. Res. 30, 1515–1527.

842   Martinec, J., 1989. Hour-to-hour snowmelt rates and lysimeter outflow during an entire

843   ablation period. Snow Cover Glacier Var. 19–28.

844   Masiokas, M.H., Villalba, R., Luckman, B.H., Le Quesne, C., Aravena, J.C., 2006.

845   Snowpack variations in the central Andes of Argentina and Chile, 1951-2005: Large-

846 scale atmospheric influences and implications for water resources in the region. J. Clim.

847 19, 6334–6352.

848 Meromy, L., Molotch, N.P., Link, T.E., Fassnacht, S.R., Rice, R., 2013. Subgrid

849 variability of snow water equivalent at operational snow stations in the western USA.

850 Hydrol. Process. 27, 2383–2400.

851 Minder, J.R., Mote, P.W., Lundquist, J.D., 2010. Surface temperature lapse rates over

852 complex terrain: Lessons from the Cascade Mountains. J. Geophys. Res. Atmospheres

853 1984–2012 115.

854 Molotch, N.P., 2009. Reconstructing snow water equivalent in the Rio Grande

855 headwaters using remotely sensed snow cover data and a spatially distributed snowmelt

856 model. Hydrol. Process. 23, 1076–1089. doi:10.1002/hyp.7206

857 Molotch, N.P., Bales, R.C., 2006. Comparison of ground-based and airborne snow

858 surface albedo parameterizations in an alpine watershed: Impact on snowpack mass

859 balance. Water Resour. Res. 42.

860 Molotch, N.P., Margulis, S.A., 2008. Estimating the distribution of snow water

861 equivalent using remotely sensed snow cover data and a spatially distributed snowmelt

862 model: A multi-resolution, multi-sensor comparison. Adv. Water Resour., Hydrologic

863 Remote Sensing 31, 1503–1514. doi:10.1016/j.advwatres.2008.07.017

864 Montgomery, D.R., Balco, G., Willett, S.D., 2001. Climate, tectonics, and the

865 morphology of the Andes. Geology 29, 579–582.

866 Neteler, M., 2010. Estimating Daily Land Surface Temperatures in Mountainous

867 Environments by Reconstructed MODIS LST Data. Remote Sens. 2, 333–351.

868 doi:10.3390/rs1020333

869   Neteler, M., Bowman, M.H., Landa, M., Metz, M., 2012. GRASS GIS: A multi-purpose

870   open source GIS. Environ. Model. Softw. 31, 124–130.

871   Newman, M., Compo, G.P., Alexander, M.A., 2003. ENSO-forced variability of the

872   Pacific decadal oscillation. J. Clim. 16, 3853–3857.

873   Núñez, J., Rivera, D., Oyarzún, R., Arumí, J.L., 2013. Influence of Pacific Ocean

874   multidecadal variability on the distributional properties of hydrological variables in

875   north-central Chile. J. Hydrol. 501, 227–240.

876   Pomeroy, J.W., Marks, D., Link, T., Ellis, C., Hardy, J., Rowlands, A., Granger, R.,

877   2009. The impact of coniferous forest temperature on incoming longwave radiation to

878   melting snow. Hydrol. Process. 23, 2513.

879   Pontailler, J.-Y., Hymus, G.J., Drake, B.G., 2003. Estimation of leaf area index using

880   ground-based remote sensed NDVI measurements: validation and comparison with two

881   indirect techniques. Can. J. Remote Sens. 29, 381–387.

882   Ragettli, S., Cortés, G., McPhee, J., Pellicciotti, F., 2014. An evaluation of approaches

883   for modelling hydrological processes in high-elevation, glacierized Andean watersheds.

884   Hydrol. Process. 28, 5674–5695. doi:10.1002/hyp.10055

885   Raleigh, M.S., Landry, C.C., Hayashi, M., Quinton, W.L., Lundquist, J.D., 2013.

886   Approximating snow surface temperature from standard temperature and humidity data:

887   New possibilities for snow model and remote sensing evaluation. Water Resour. Res.

888   49, 8053–8069.

889   Rankinen, K., Karvonen, T., Butterfield, D., 2004. A simple model for predicting soil

890   temperature in snow-covered and seasonally frozen soil: model description and testing.

891   Hydrol. Earth Syst. Sci. Discuss. 8, 706–716.

892   Rhee, J., Im, J., 2014. Estimating high spatial resolution air temperature for regions with

893   limited in situ data using MODIS products. Remote Sens. 6, 7360–7378.

894   Rice, R., Bales, R.C., 2010. Embedded-sensor network design for snow cover

895   measurements around snow pillow and snow course sites in the Sierra Nevada of

896   California. Water Resour. Res. 46.

897   Rittger, K., Painter, T.H., Dozier, J., 2013. Assessment of methods for mapping snow

898   cover from MODIS. Adv. Water Resour. 51, 367–380.

899   Rubio-Álvarez, E., McPhee, J., 2010. Patterns of spatial and temporal variability in

900   streamflow records in south central Chile in the period 1952–2003. Water Resour. Res.

901   46, W05514. doi:10.1029/2009WR007982

902   Salazar, G., Raichijk, C., 2014. Evaluation of clear-sky conditions in high altitude sites.

903   Renew. Energy 64, 197–202.

904   Scheel, M.L.M., Rohrer, M., Huggel, C., Santos Villar, D., Silvestre, E., Huffman, G.J.,

905   2011. Evaluation of TRMM Multi-satellite Precipitation Analysis (TMPA) performance

906   in the Central Andes region and its dependency on spatial and temporal resolution.

907   Hydrol Earth Syst Sci 15, 2649–2663. doi:10.5194/hess-15-2649-2011

908   Searcy, J.K., Hardison, C.H., 1960. Double-mass curves.

909   Sicart, J.E., Essery, R.L., Pomeroy, J.W., Hardy, J., Link, T., Marks, D., 2004. A

910   sensitivity study of daytime net radiation during snowmelt to forest canopy and

911   atmospheric conditions. J. Hydrometeorol. 5, 774–784.

912   Slater, A.G., Barrett, A.P., Clark, M.P., Lundquist, J.D., Raleigh, M.S., 2013.

913   Uncertainty in seasonal snow reconstruction: Relative impacts of model forcing and

914 image availability. Adv. Water Resour., Snow–Atmosphere Interactions and

915 Hydrological Consequences 55, 165–177. doi:10.1016/j.advwatres.2012.07.006

916 Tarboton, D.G., Luce, C.H., 1996. Utah energy balance snow accumulation and melt

917 model (UEB). Citeseer.

918 Vera, C., Silvestri, G., Liebmann, B., González, P., 2006. Climate change scenarios for

919 seasonal precipitation in South America from IPCC-AR4 models. Geophys. Res. Lett.

920 33.

921 Vicuña, S., Garreaud, R.D., McPhee, J., 2011. Climate change impacts on the

922 hydrology of a snowmelt driven basin in semiarid Chile. Clim. Change 105, 469–488.

923 doi:10.1007/s10584-010-9888-4

924 Wan, Z., Zhang, Y., Zhang, Q., Li, Z., 2002. Validation of the land-surface temperature

925 products retrieved from Terra Moderate Resolution Imaging Spectroradiometer data.

926 Remote Sens. Environ. 83, 163–180.

927 Wan, Z., Zhang, Y., Zhang, Q., Li, Z.-L., 2004. Quality assessment and validation of

928 the MODIS global land surface temperature. Int. J. Remote Sens. 25, 261–274.

929 Williamson, S.N., Hik, D.S., Gamon, J.A., Kavanaugh, J.L., Flowers, G.E., 2014.

930 Estimating temperature fields from MODIS land surface temperature and air

931 temperature observations in a sub-Arctic Alpine environment. Remote Sens. 6, 946–

932 963.

933

934   List of Tables

944

945

946 **Table 1. Study area subdivision, relevant characteristics and model parameters**

Cluster	Area x10^3 [km^2]	Average elevation [m.a.s.l.]	Average cluster latitude [°]	Clear sky Index (Kc)	Avg. a_r [cm/°C/day]	T_a [°C]	Forest Cover [%]
C1	26.5	3300	-29.4	0.78	0.02	18.3	2.0
C2	17.9	2760	-33.7	0.89	0.11	16.1	5.5
C3	9.20	1890	-36.4	0.83	0.18	12.2	13.8
C4	49.3	3520	-30.1	0.8	0.04	20.4	1.4
C5	18.5	2855	-33.4	0.83	0.15	15.6	3.0
C6	7.60	2807	-34.8	0.83	0.21	13.9	2.3
C7	14.8	2167	-36.1	0.85	0.20	16.7	2.5
C8	8.30	1840	-37.0	0.82	0.23	15.7	4.9
Total / Average	152.1	2320	***	0.83	0.14	***	3.3

947

948

949 **Table 2. Snow pillow measurements available within the study domain**

950

ID	SWE data	Symbol	Lat. (S)	Long. (W)	Elevation [m.a.s.l.]	Reference cluster
CHILE						
1	Quebrada Larga	QUE	30° 43'	70° 16'	3500	C1
2	Cerro Vega Negra	CVN	30° 54'	70° 30'	3600	C1
3	El Soldado	SOL	32° 00'	70° 19'	3290	C2
4	Portillo	POR	32° 50'	70° 06'	3000	C2
5	Laguna Negra	LAG	33° 39'	70° 06'	2780	C2
6	Lo Aguirre	LOA	35° 58'	70° 34'	2000	C3
7	Alto Mallines	ALT	37° 09'	70° 14'	1770	C3
ARGENTINA						
8	Toscas	TOS	33° 09'	69° 53'	3000	C5
9	Laguna Diamante	DIA	34° 11'	69° 41'	3300	C6
10	Laguna Atuel	ATU	34° 30'	70° 02'	3420	C6
11	Valle Hermoso	VAL	35° 08'	70° 12'	2250	C7
12	Paso Pehuenches	PEH	35° 08'	70° 23'	2545	C7

951

952

953 **Table 3. Summary of snow depth and density intensive study campaigns**

954

Year	ID (Figure 1)	Symbol	Field site	Date	Snow-pit density [kg/m^3]	SWE average [mm]	SWE std. dev. [mm]	SWE range [mm]	Sample size
2010	2	ODA	Ojos de Agua	25-sep	352	450	163	848 - 0	134
2011	2	ODA	Ojos de Agua	30-ago	341	705	199	1194 - 136	374
	5	MOR	Morales	01-sep	367	642	282	1101 - 0	171
	8	OBL	Olla Blanca DET	31-ago	333	539	217	1032 - 79	289
2012	1	CVN	Cerro Vega Negra	28-ago	308	296	115	700 - 40	166
	3	MAR	Juncal - Mardones	30-ago	373	530	230	1120 - 40	163
	5	MOR	Morales	12-sep	412	590	360	1240 - 150	152
	8	OBL	Olla Blanca DET	03-sep	411	590	260	1230 - 0	309
	4	POR	Portillo	15-sep	410	170	180	1230 - 0	181
2013	1	CVN	Cerro Vega Negra	21-ago	356	405	165	1040 - 10	282
	2	ODA	Ojos de Agua	23-ago	355	540	220	1310 - 100	300
	10	CHI	Nevados Chillán[a]	27-ago	416	980	240	1270 - 30	104
	10	CHI	Nevados Chillán[b]	27-ago	416	600	240	1230 - 70	216
	4	POR	Portillo	23-ago	392	340	210	1120 - 0	91
	6	LAG	Laguna Negra	30-ago	455	480	250	1770 - 0	32
2014	1	CVN	Cerro Vega Negra	05-ago	321	163	85	620 - 0	326
	5	MOR	Morales	12-ago	401	510	250	1190 - 0	329
	7	LVD	Lo Valdez	13-ago	365	710	290	1260 - 0	186
	8	OBL	Olla Blanca DET	12-sep	363	420	240	1210 - 0	334
	9	RBL	Río Blanco DET	06-sep	354	620	290	1210 - 0	99
	10	CHI	Nevados Chillán[a]	26-sep	504	830	400	380 - 1510	18
	10	CHI	Nevados Chillán[b]	26-sep	504	980	250	530 - 1500	87
	4	POR	Portillo	19-ago	436	170	140	850 - 0	73
	6	LAG	Laguna Negra	30-ago	365	300	110	540 - 0	117

(a) without forest cover (upper part of basin).
(b) with of forest cover (lower part of basin).

955

956

957

958 **Table 4. Model validation statistics against intensive study area observations around snow pillows**
959 **and at catchment scale**

960

	Reconstructed SWE vs. MODIS pixel (grid) sampling (selected snow-pillows)						
	Avg. Sampling [mm] (1)	Std. Dev. Sampling [mm] (2)	Avg. Model [mm] (3)	SP (sensor) [mm] (4)	RE$_\%$ (avg.) (1) vs. (3)	RE$_\%$ (avg.) (1) vs. (4)	RE$_\%$ (avg.) (3) vs. (4)
CVN	223	110	334	200	49%	-10%	98%
POR	227	177	170	353	-25%	35%	-51%
LAG	395	180	283	280	-28%	-30%	8%
	Reconstructed SWE vs. snow surveys (pilot-basins)						
	avg. Sampling [mm] (1)	std. dev. Sampling [mm] (2)	avg. Model [mm] (3)	std. dev. Model [mm] (4)	RE$_\%$ (avg.) (1) vs. (3)	RE$_\%$ (std. dev.) (2) vs. (4)	
CVN	253	133	298	63	18%	-53%	
ODA-MAR	556	203	535	128	-4%	-37%	
MOR-LVD	613	295	375	115	-39%	-61%	
OBL-RBL	497	252	317	89	-36%	-65%	
CHI (forest)	790	245	257	46	-67%	-81%	
CHI (clear)	905	320	724	170	-20%	-47%	
	Reconstructed SWE vs. snow -pillows (Sep 1 – Chile & Oct 1 – Argentina)						
	R^2	Slope	Intercept [mm]	SE$_{\bar{x}}$ [mm]	RE$_\%$	RMSE [mm]	Mod. SWE average [mm]	Mod. SWE std. dev. [mm]
QUE	0.71	1.39	131	208	79	335	529	350
CVN	0.78	0.92	247	140	56	251	609	281
SOL	0.68	0.85	-16	112	-19	127	401	241
POR	0.32	0.52	87	277	-36	398	437	324
LAG	0.42	0.76	16	217	-21	230	424	263
LOA	0.88	0.79	101	123	-5	171	734	316
ALT	0.83	0.56	5	89	-41	332	489	296
TOS	0.78	0.41	26	72	-52	251	120	141
DIA	0.76	0.85	38	141	-4	137	455	291
ATU	0.56	1.04	77	378	9	349	1263	496
VAL	0.72	0.74	11	211	-24	273	457	371
PEH	0.74	1.01	303	334	32	436	1302	580
Average	0.68			192	-2	274	602	330

961

962

963 **Table 5. Coefficient of determination R^2 between river melt season flows (SSRV), estimated and**
964 **observed SWE (end-of-winter).**

965

	R2 values specific SSRV vs. Estimated SWE per cluster		R2 values specific SSRV vs. SWE at snow pillows (2001 – 2013)*	
	2001 - 2014	Neglecting 2009 at Argentinean clusters**	Best	2nd best
c1	0.84	***	0.74 (CVN)	0.69 (QUE)
c2	0.78	***	0.82 (LAG)	0.68 (POR)
c3	0.57	***	0.17 (LOA)	0.16 (ALT)
c4	0.87	***	***	-
c5	0.66	0.82	0.81 (TOS)	-
c6	0.45	0.76	0.87 (ATU)	0.77 (DIA)
c7	0.64	0.89	0.77 (VAL)	0.41 (PEH)
c8	0.48	0.64	***	-

966 *** 2014 flows in Argentina unavailable to us at the moment of writing.**
967 **** 2009 is considered an outlier year for the reconstruction at Argentinean sites.**
968

Table 6. Peak SWE 2001 - 2014 climatology for river basins within the study region. Basin-wide averages, SCA-wide averages and basin-wide water volumes shown

971

ID	Basin - gauge station	Lat. S	Long. W	Outlet Elev. [m .a.s.l..]	Area [km²]	SWE		
						Basin-wide [mm]	Over-SCA [mm]	Basin-wide [m³x10⁻⁶]
	CHILE							
1	Copiapó en Pastillo	27° 59'	69° 58'	1300	7470	45	120	336
2	Huasco en Algodones	28° 43'	70° 30'	750	7180	68	161	488
3	Elqui en Algarrobal	29° 59'	70° 35'	760	5710	151	269	862
4	Hurtado en San Agustín	30° 27'	70° 32'	2050	676	302	325	204
5	Grande en Puntilla San Juan	30° 41'	70° 55'	2140	3545	137	306	486
6	Cogotí en La Fraguita	31° 06'	70° 53'	1021	491	182	335	89
7	Illapel en Huintil	31° 33'	70° 57'	650	1046	180	305	188
8	Chalinga en San Agustín	31° 41'	70° 43'	920	437	142	332	62
9	Choapa en Salamanca	31° 48'	70° 55'	560	2212	214	356	473
10	Sobrante en Piñadero	32° 12'	70° 42'	2057	126	172	198	22
11	Alicahue en Colliguay	32° 18'	70° 44'	852	344	92	184	32
12	Putaendo en Resg. Los Patos	32° 30'	70° 34'	1218	890	273	346	243
13	Aconcagua en Chacabuquito	32° 51'	70° 30'	950	2110	609	692	1285
14	Mapocho en Los Almendros	33° 22'	70° 27'	970	640	269	342	172
15	Maipo en El Manzano	33° 35'	70° 22'	850	4840	692	760	3349
16	Cachapoal en Puente Termas	34° 15'	70° 34'	700	2455	700	814	1719
17	Tinguiririca en Los Briones	34° 43'	70° 49'	560	1785	532	677	950
18	Teno en Claro	34° 59'	70° 49'	650	1210	438	524	530
19	Lontué en Colorado - Palos	35° 15'	71° 02'	600	1330	656	759	872
20	Maule en Armerillo	35° 42'	70° 10'	470	5465	525	554	2869
21	Ñuble en San Fabián	36° 34'	71° 33'	410	1660	376	430	624
22	Polcura en Laja	37° 19'	77° 32'	675	2088	358	378	748
	ARGENTINA							
23	Jachal en Pachimoco	30° 12'	68° 49'	1563	24266	79	175	1917
24	San Juan en km 101	31° 15'	69° 10'	1129	23860	308	569	7349
25	Mendoza en Guido	32° 54'	69° 14'	1479	7304	460	672	3360
26	Tunuyán en Zapata	33° 46'	69° 16'	852	11230	289	592	3245
27	Diamante en La Jaula	34° 40'	69° 18'	1451	19332	395	489	7636
28	Atuel en Loma Negra	35° 15'	69° 14'	1353	3696	338	525	1249
39	Malargue en La Barda	35° 33'	69° 40'	1568	1055	171	284	180
30	Colorado en Buta Ranquil	37° 04'	69° 44'	817	14896	288	495	4290
31	Neuquén en Rahueco	37° 21'	70° 27'	870	8266	356	446	2943

972

973

1010 Figure 12. Restricted Degree Day factor as a function of space (basin cluster) and
1011 climatological properties. Bowen (β) coefficient shown between parenthesis in legend.
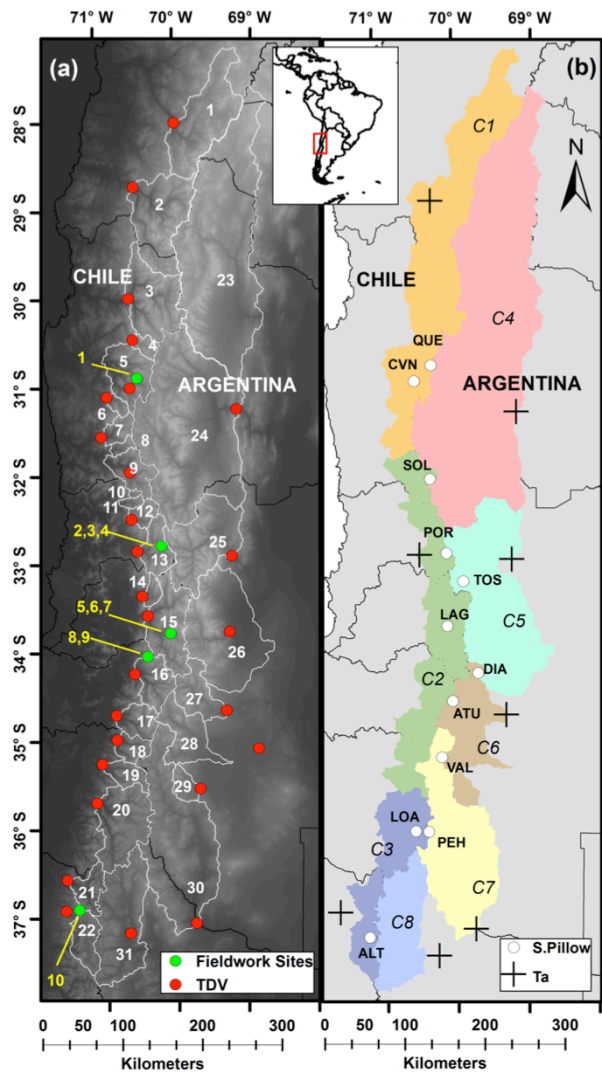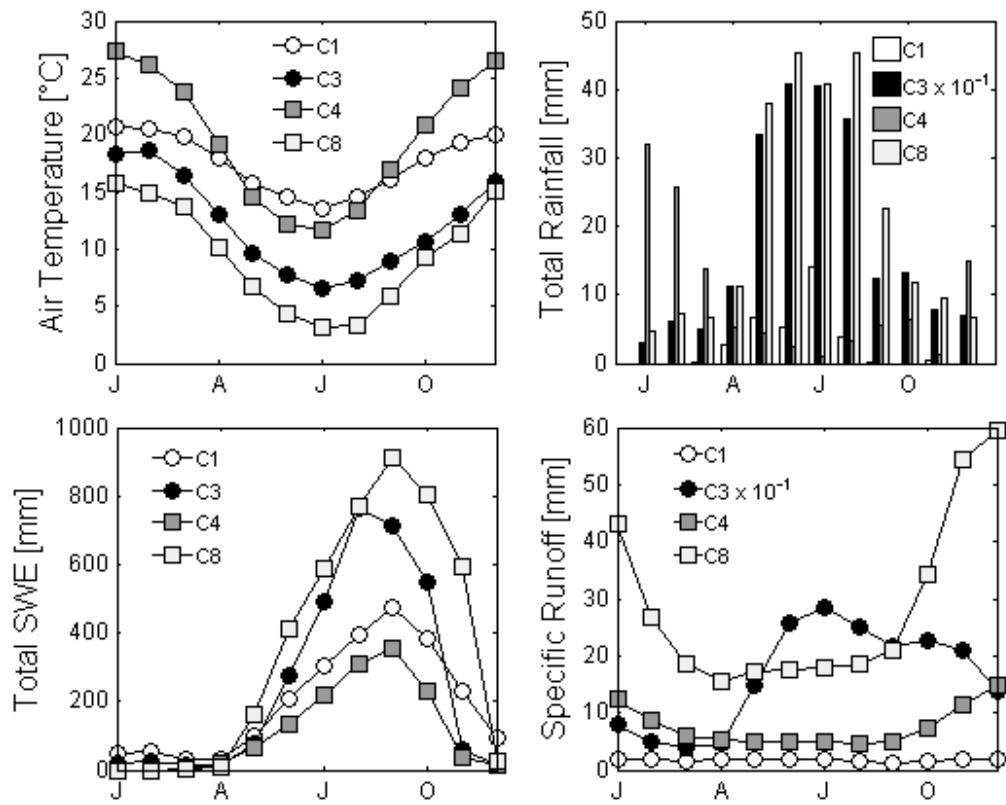
1012

1

Figure 1. Study area and model domain: (a) river basins, stream gages (red circles) and sites where snow survey data are available (green circles), (b) hydrologic units (C1 to C8) and snow-pillow stations (white circles).

Figure 2. Summarized hydro-climatology of the model domain. Data from meteorological stations located within zones C1, C4, C3 and C8 summarized the hidro-climatological regime of northern-west, northern-east, southern-west and southern-east zones respectively. Total SWE is SWE measured at selected snow pillow stations.

11
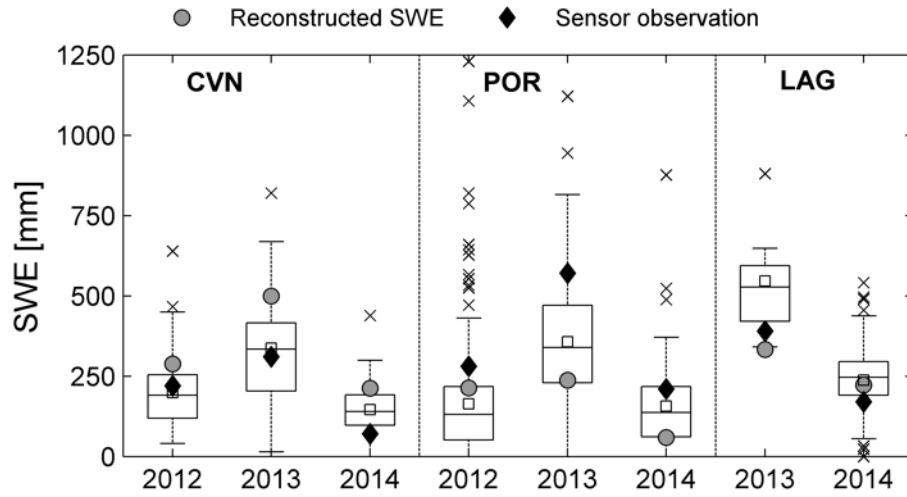
Figure 2. Reconstructed SWE validation at selected snow-pillow sites. Black diamonds are instrumental records, gray circles are model estimates, and box-plots summarize manual verification dataset around the pillow site. Upper and lower box limits are the 75% and 25% quartiles, horizontal line is the median, white box is the mean, upper and lower dashes represent plus and minus 2.5 standard deviations from the mean, and crosses are outlying values.

17

18
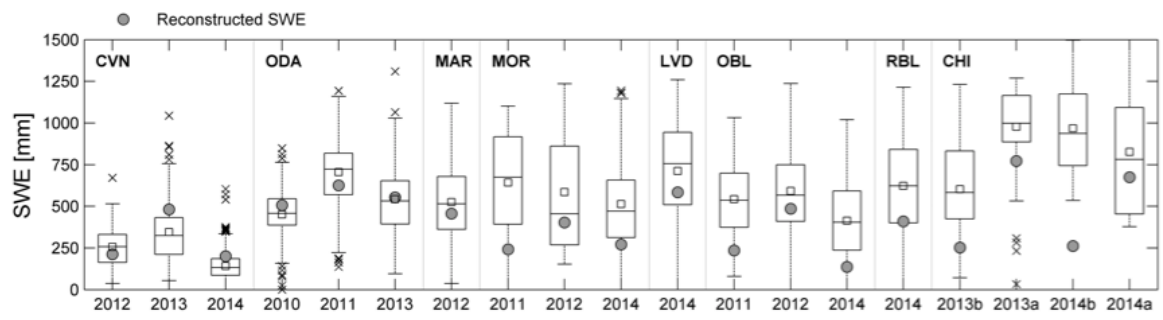
19 **Figure 3. Reconstructed SWE validation at pixels with snow survey data. Box plots summarize all**
20 **individual measurements at pixels co-located with SWE reconstruction. Symbology analogous to**
21 **Figure 2.**
22

23
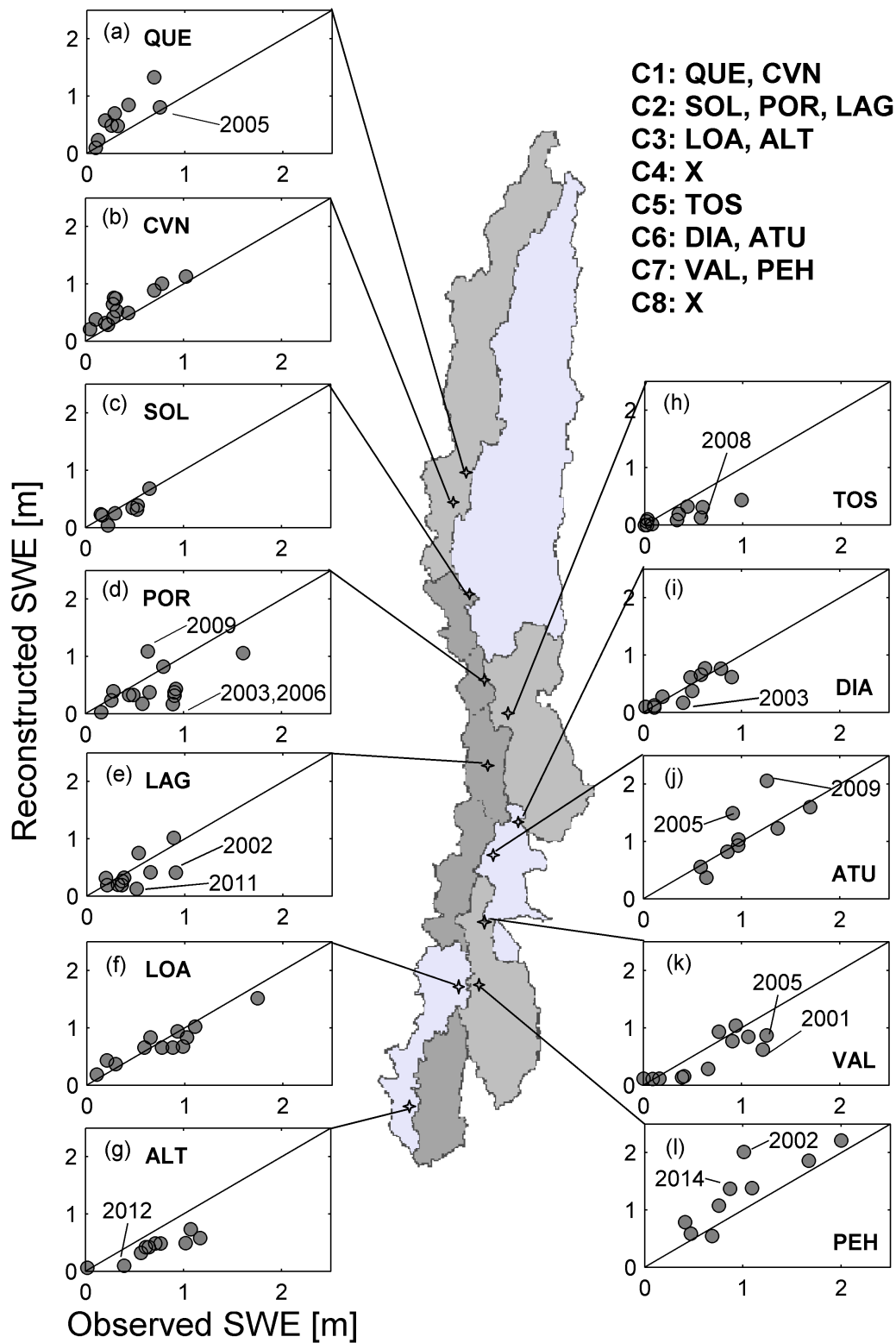
Figure 4. Comparison between peak reconstructed and observed SWE at snow-pillow sites. Solid line represents the 1:1 line.
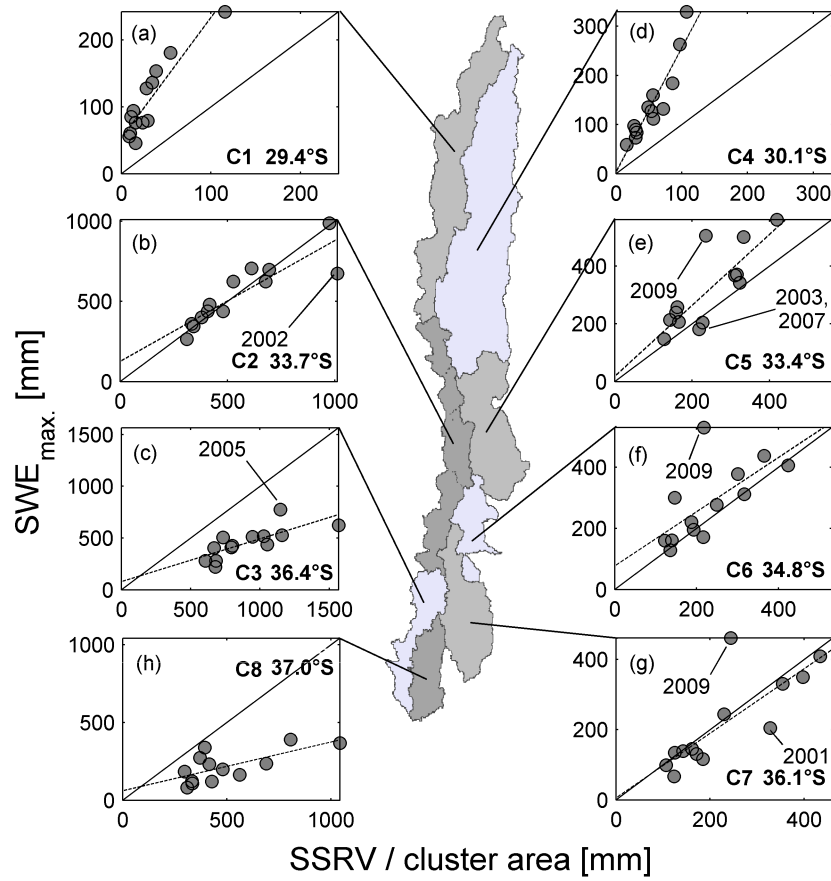
Figure 5. Area-specific spring - summer runoff volume (SSRV) versus peak SWE. Clusters 1 through 3 include rivers on the Chilean (western) slope of the Andes range; clusters 4 through 8 correspond to Argentinean (eastern) rivers. Solid line represents 1:1 line. C4 and C8 SSRV by precipitation-area regressions.
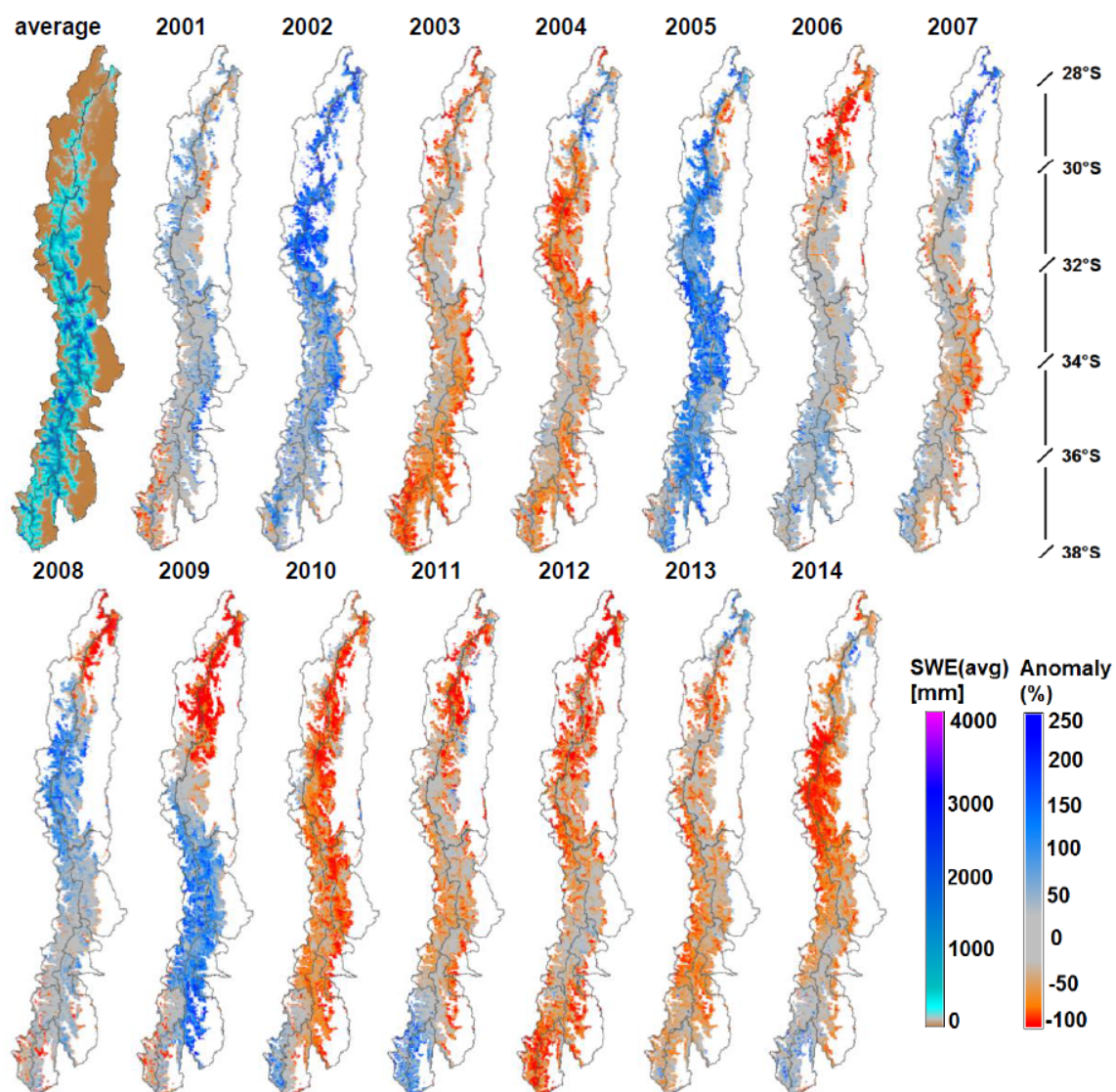
Figure 6. Regional peak (Sep 1st) SWE Climatology for the 2001 - 2014 period (upper left panel), and annual peak SWE anomalies.

37
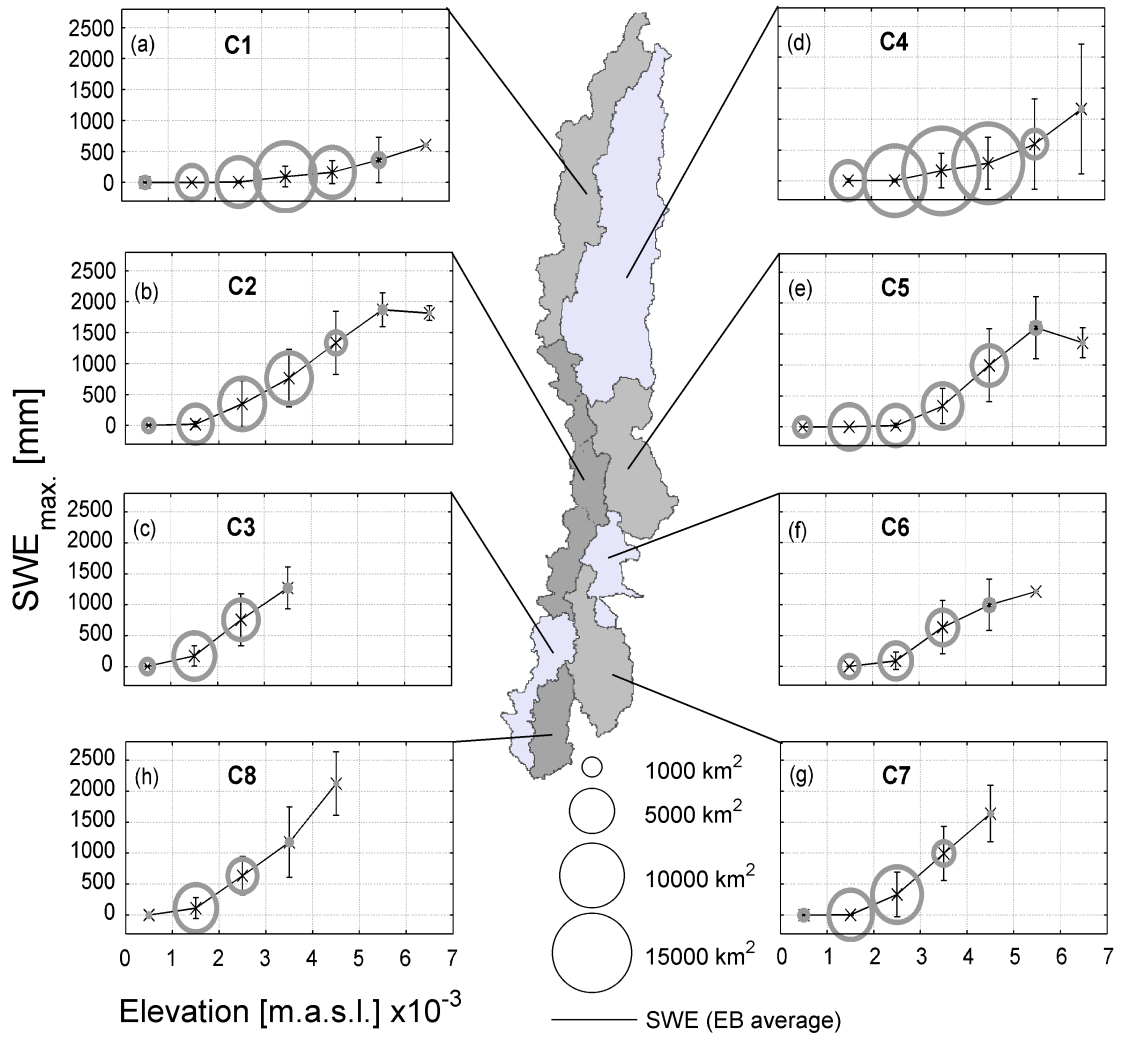
Figure 7. Maximum SWE through 1000 m elevation bands (EB). Crosses are mean values within EB, lines are estimated DEM-elevation profile. Circle areas are proportional to EB areas [km2].

38
39

40

8
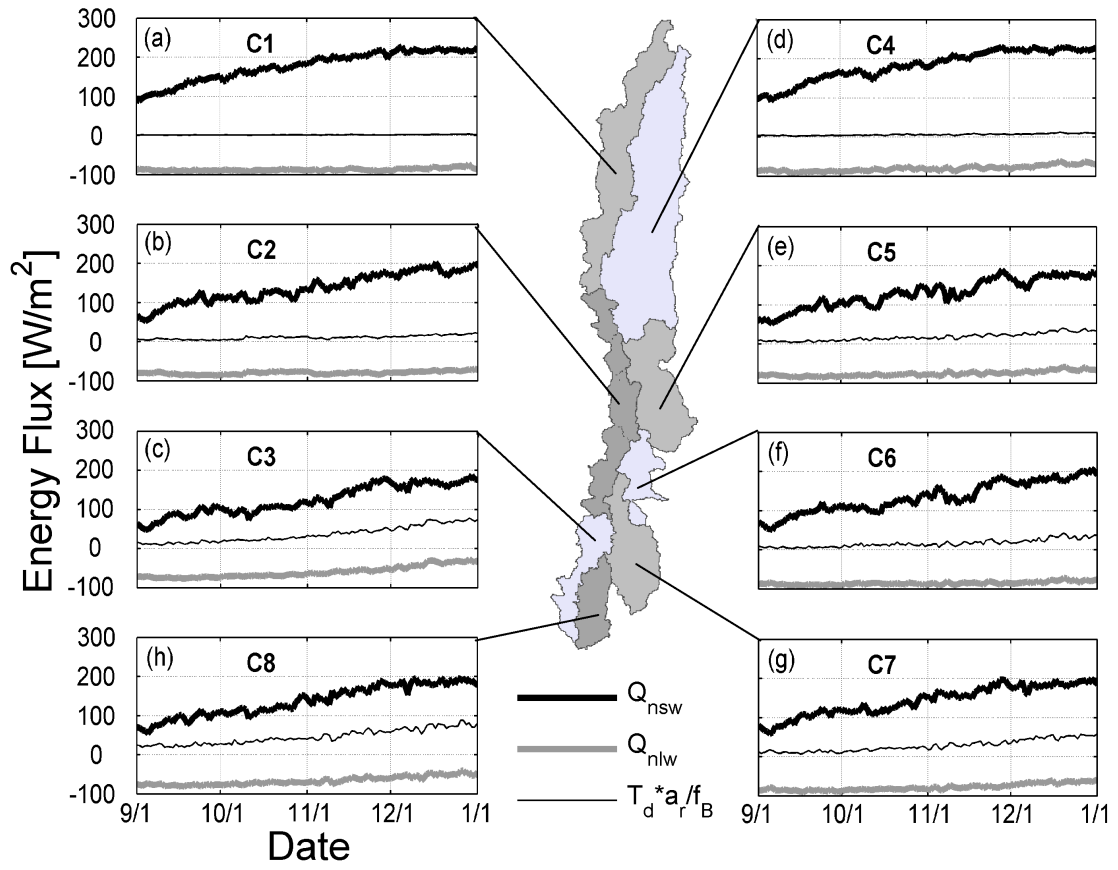
Figure 8. Time series of energy fluxes over snow surface (average over 14 years) and global average per cluster. Unique axes scale for all plots.
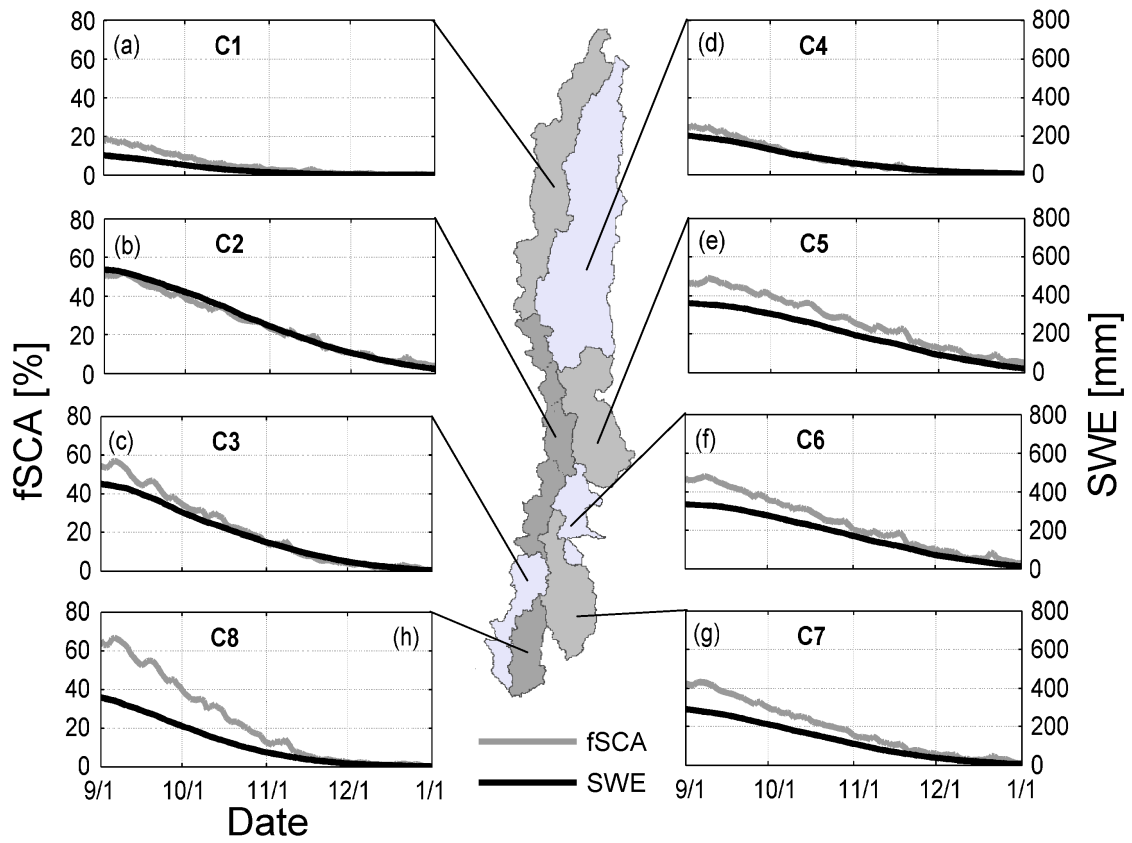
Figure 9. Average seasonal evolution of fSCA and SWE in the study region. Lower right panel shows the spatial correlation between time-averaged fSCA, SWE and specific melt-season river discharge.
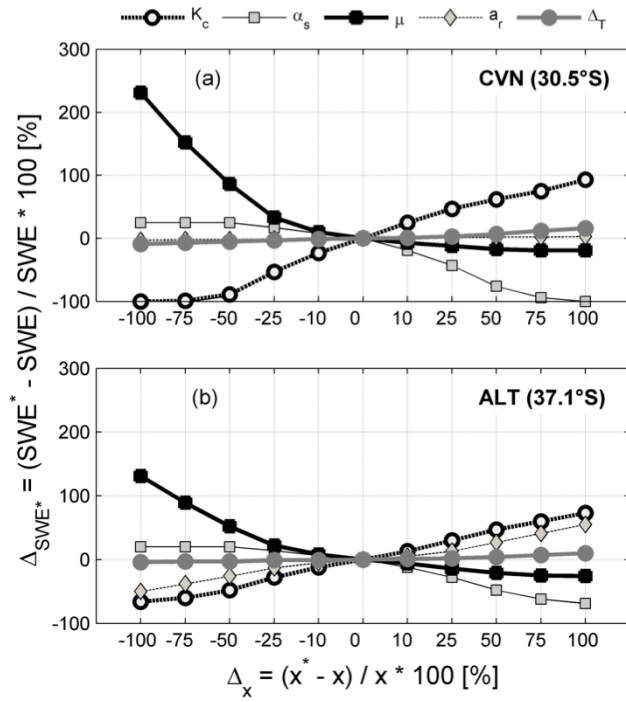
50

Figure 10. Sensitivity of peak SWE estimates to model forcings and parameters. Average over the 2001 - 2014 period at selected snow pillow sites. Δ_x represents the percentage change over each parameter studied respect to the base case.
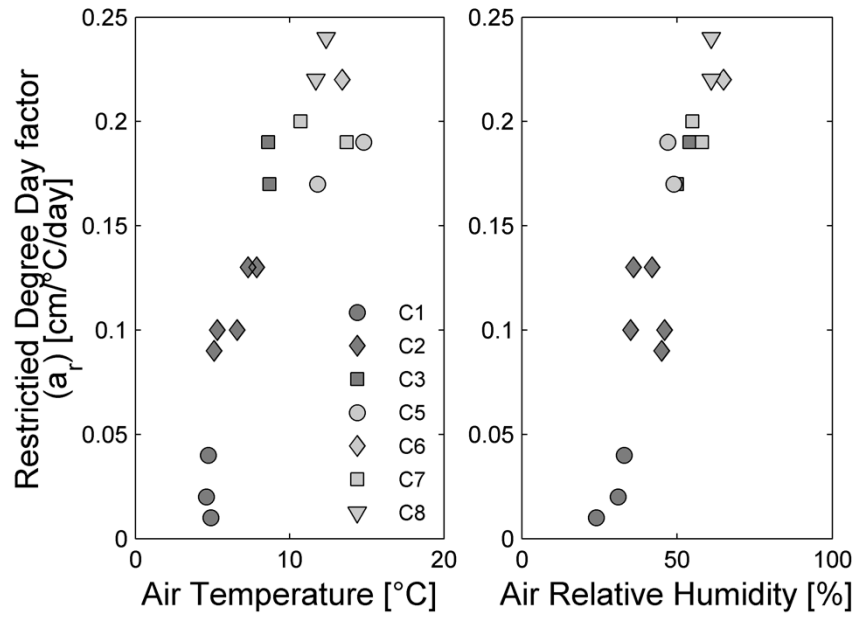
55

Figure 11. Restricted Degree Day factor as a function of space (basin cluster) and climatological properties. Bowen (β) coefficient shown between parenthesis in legend.